

## Chapter 9

### Radio frequency scanning probe measurements of materials

#### 9.1. Electromagnetic characterization of materials: fundamental concepts

Preceding chapters have described the near field scanning microwave microscope (NSMM), while discussing both the underlying theory of operation and practical considerations for instrumentation. A primary application area for NSMMs and related microscopes is broadband, local metrology of materials with nanometer-scale spatial resolution. Several methods for spatially-resolved characterization of materials are reviewed in this chapter. We begin by reviewing the fundamental concepts of electromagnetic materials metrology. Furthermore, since the extraction of quantitative information from NSMM measurements requires appropriate modeling of the measurement system, we will describe strategies for modeling probe-material interactions. Once the fundamental concepts and models have been established, we will review several applications of scanning-probe-based metrology to local characterization of electromagnetic materials.

Just as Maxwell's equations are fundamental to the characterization of electromagnetic devices, they are also fundamental to electromagnetic characterization of materials. In Chapter 2, we introduced the Maxwell-Lorentz microscopic equations. To proceed from the microscopic equations to a description of electromagnetic fields in materials, it is reasonable to start with the introduction of the constitutive relations for polarization and magnetization. In addition to the time-dependent charge and current distributions, the Maxwell-Lorentz equations also require specification of the relationship between the polarization  $\mathbf{P}$ , magnetization  $\mathbf{M}$ , and the electromagnetic fields  $\mathbf{E}$  and  $\mathbf{B}$ , as well as their space and time derivatives. These relations are called constitutive relations. Note that the magnetization and polarization may each depend on both the electric and magnetic fields. While these concepts are especially useful for emerging materials like ferromagnetic-ferroelectric composites, photonic bandgap crystals, or metamaterials, each class of materials may require a customized approach. Therefore, it is important to have a fundamental understanding of the constitutive relations in Maxwell's equations. In general, the primary objective is to describe the general electromagnetic response of a material, starting from the microscopic quantities and subsequently averaging to get the macroscopic quantities. This chapter is primarily concerned with the local, spatially-resolved measurement techniques of spatially varying quantities at small length scales. Techniques for macroscopic microwave measurements of dielectric properties and techniques for electromagnetic characterization of bulk materials are addressed in numerous texts [1]-[4].

The constitutive relations can be expressed in the form

$$\mathbf{P} \Leftrightarrow \{\mathbf{E}, \mathbf{B}\}, \quad \mathbf{M} \Leftrightarrow \{\mathbf{B}, \mathbf{E}\} \quad , \quad (9.1)$$

where  $\Leftrightarrow$  indicates that this relationship can be either local or nonlocal in both time and space. Further, these relations can be either linear or nonlinear functions of the driving fields [1]. Note that the dielectric polarization is odd under parity transformation and even under time reversal while the magnetization is

even under parity transformation and odd under time reversal. Although  $\mathbf{E}$  and  $\mathbf{B}$  are widely accepted as fundamental fields, here we will use  $\mathbf{E}$  and  $\mathbf{H}$  as driving fields that may be time dependent.

The introduction of constitutive relations for polarization and magnetization gives rise to complications due to the fact that they depend not only on the applied fields but also on the internal energy of the investigated material in its given state. In the case of magnetization, the response originates from moving charge and spin, as described by Bloch or Landau-Lifshitz equations [3]. These phenomenological equations relate the time-dependent magnetization to both the external magnetic field and the internal energy. The behavior of dielectric materials originates from charge as well electric multipole moments. The description of the time-dependent polarization response is more complex because the motion of charges and multipoles induces magnetic fields in the material in addition to electric fields. Furthermore, under ambient conditions only a small percentage of electric dipoles are fully aligned with an applied electric field due to thermal effects. Naturally, the situation becomes even more complicated in composite materials. For example, in magneto-electric materials, complex coupling mechanisms include the electric-field-induced shift of the Landé  $g$  factor, spin-orbit interactions, exchange energies and the electric-field-induced shift of single ion anisotropy energies [5], [6]. The general approach presented here follows References [7] and [8] and includes the possibility of magneto-electric coupling within the material, but the results can be extended to materials without such coupling. For micro- or nanoscale materials, the microscopic approach is necessary, however some problems in RF nanoelectronics can be treated by averaging the microscopic quantities to find macroscopic quantities that can be used instead.

The standard materials relations in Maxwell's equations are often expressed in terms of the effective macroscopic polarization and magnetization. The magnetic induction is related to the magnetic field  $\mathbf{H}$  and the magnetization  $\mathbf{M}$  by

$$\mathbf{B} = \mu_0(\mathbf{H} + \mathbf{M}) \quad , \quad (9.2)$$

while the electric displacement is related to the electric field polarization and the macroscopic quadrupole density  $\tilde{\mathbf{Q}}$  by

$$\mathbf{D} = \varepsilon_0\mathbf{E} + \tilde{\mathbf{P}} - \nabla \cdot [\tilde{\mathbf{Q}}] = \varepsilon_0\mathbf{E} + \mathbf{P} \quad . \quad (9.3)$$

$\tilde{\mathbf{P}}$  is the macroscopic dipole density, while  $\varepsilon_0$  and  $\mu_0$  are the permittivity and permeability of free space, respectively. In order to move from the macroscopic variables to the microscopic variables, we define the macroscopic variables in terms of microscopic densities. The microscopic dipole density with the quadrupole-moment distribution for  $N$  particles is

$$\mathbf{p} = \sum_{j=1}^N \mathbf{r}_j e_j \delta(\mathbf{r} - \mathbf{r}_j) - \frac{1}{2} \sum_{j=1}^N e_j (\mathbf{r}_j \mathbf{r}_j) \nabla \delta(\mathbf{r} - \mathbf{r}_j) = \sum_j \mathbf{p}_j \quad . \quad (9.4)$$

The index  $j = 1, 2, \dots, N$ . The position of the  $j$ -th particle is  $\mathbf{r}_j$ . The charge on the  $j$ -th particle  $e_j$  can be positive or negative. The summation is over the bound charge, which is electrically neutral as a whole. The same condition also applies to the free charge. The motion of the free charge gives rise to kinetic energy that has to be included in the internal energy of the system. Similarly, the microscopic magnetic dipole density is

$$\mathbf{m} = \sum_i \left\{ \gamma_i \mathbf{s}_i(\mathbf{r}_i) \delta(\mathbf{r} - \mathbf{r}_i) - \frac{\gamma_{ei}}{e_i} \boldsymbol{\pi}_i \times \mathbf{p}_i \right\} \equiv \sum_i \mathbf{m}_i + \mathbf{m}_0 \quad . \quad (9.5)$$

Equation (9.5) clearly separates the magnetic dipole density into contributions from spin and from charge motion.

The gyromagnetic ratio is

$$\gamma_i = g_i \mu_0 e_i / 2m_{si} \quad , \quad (9.6)$$

where  $m_{si}$  is the mass of the electron,  $g_i$  is the spectroscopic Landé factor and  $\mathbf{s}$  is the intrinsic spin. In addition,

$$\gamma_{ei} = \mu_0 e_i / 2m_{si} \quad (9.7)$$

and the canonical momentum is given by

$$\boldsymbol{\pi}_i = m_{si} \frac{d\mathbf{r}_i}{dt} + e_i \mathbf{A}_i \quad , \quad (9.8)$$

where  $\mathbf{A}_i$  is the vector potential. The expected values of macroscopic polarization and magnetization are found by averaging:

$$\mathbf{P}(\mathbf{r}, t) = \langle \mathbf{p} \rangle = Tr[\mathbf{p}\rho(t)] \quad (9.9a)$$

$$\mathbf{M}(\mathbf{r}, t) = \langle \mathbf{m} \rangle = Tr[\mathbf{m}\rho(t)] = \sum_i \langle \mathbf{m}_i \rangle (\mathbf{r}, t) + \langle \mathbf{m}_0 \rangle (\mathbf{r}, t) \quad , \quad (9.9b)$$

where  $\rho(t)$  is the statistical density operator satisfying Liouville's equations and  $Tr(.)$  is the trace operator. Note that both  $\mathbf{p}$  and  $\mathbf{m}$  implicitly depend on functions of electric and magnetic field. By use of statistical mechanics, it is possible to derive the evolution equations for equilibrium and non-equilibrium conditions and the corresponding equations of motion for the magnetization and polarization, including the cross-coupling terms. Such a comprehensive derivation is beyond the scope of this chapter, but leads to the classical Landau-Lifshitz equation of motion for magnetization and the equation of motion for polarization. For the interested reader, the details of the derivation can be found in Reference [7].

More complex interactions such as magneto-electric interactions may be incorporated into the equations of motion by including all possible relationships between the polarization and magnetization with the magnetic and electric fields. The macroscopic averages of the microscopic variables that are useful for measurement applications are [8]

$$\mathbf{P} \approx \alpha_{ee} \mathbf{E}_p + \alpha_{em} \mathbf{H}_m + \chi_{es} \cdot [\boldsymbol{\Sigma}_\epsilon] + \chi_{eu} (T - T_0) \quad , \quad (9.10a)$$

$$\mathbf{M} \approx \alpha_{me} \mathbf{E}_p + \alpha_{mm} \mathbf{H}_m + \chi_{ms} \cdot [\boldsymbol{\Sigma}_\epsilon] + \chi_{mu} (T - T_0) \quad , \quad (9.10b)$$

with

$$\mathbf{E}_p(\mathbf{r}, t) \approx [\chi_{ee}]^{-1} \cdot \mathbf{P}(\mathbf{r}, t) + [\mathbf{N}_p] \cdot \mathbf{P}(\mathbf{r}, t) \quad , \quad (9.11a)$$

$$\mathbf{H}_m(\mathbf{r}, t) \approx [\chi_{mm}]^{-1} \cdot \mathbf{M}(\mathbf{r}, t) + [\mathbf{N}_m] \cdot \mathbf{M}(\mathbf{r}, t) \quad (9.11b)$$

The tensors  $[\chi_{ii}]$  are the electric and magnetic susceptibility tensors while the tensors  $[\mathbf{N}_i]$  are depolarization and demagnetization tensors. The coefficients  $\alpha_{ij}$  are the corresponding magneto-electric coupling coefficients. The tensor  $[\Sigma_\epsilon]$  represents the influence of strain. Finally, within a material the macroscopic fields differ from applied fields due to induced surface depolarization charges. For example, the total electric field can be expressed as

$$\mathbf{E}_p(\mathbf{r}, t) = \mathbf{E}_0(\mathbf{r}, t) - [\mathbf{N}_p] \cdot \mathbf{P}(\mathbf{r}, t), \quad (9.12)$$

where  $\mathbf{E}_0$  is the applied field.

This brief introduction of the microscopic electromagnetic field variables provides a foundation for describing complex materials at sub-micrometer length scales. The application of this analysis to specific cases can be quite challenging, requiring detailed knowledge of the relevant geometrical configurations and boundary conditions. The definitions of the electromagnetic field variables for microscopic characterization of materials that we have introduced here provide but a starting point for extending the theory to each particular case. Some insightful examples are described in Reference [3].

## 9.2. Impedance circuit models of probe-sample interactions

### 9.2.1 Toward materials characterization with near-field scanning microwave microscopy

We now focus on models that enable quantitative characterization of device and material properties by use of an NSMM. In Chapter 8, we discussed the interaction of the tip with the measured sample under test (SUT) or device under test (DUT) when the NSMM probe tip was at a certain distance above the surface. We introduced the coupling capacitance and approaches to extract quantitative, calibrated data from the measurements. Here, we extend the models to incorporate material properties. Materials measurements performed by use of an NSMM usually come in one of two forms: height-dependent measurements with the lateral position of the tip fixed or spatially-resolved NSMM images. For the latter case, we will focus primarily on images obtained in “contact mode,” i.e. with the probe in direct mechanical and electrical contact with the SUT.

Recall that for NSMMs that are configured as a one-port system, the measured parameter is the reflection coefficient. The transmission coefficient is an additional measured parameter for two-port NSMM systems. Also recall that in a NSMM, the tip-sample interaction is in the near field. In most cases the wavelength of the applied field is much larger than the interaction dimensions and the sample dimensions are large with respect to the tip dimensions. Thus, the modeling of the probe’s interaction with a material or device is often done using lumped-element impedance circuits. If it is necessary to consider propagation between two ports in a measurement system, then a transmission line model, or a hybrid combination of lumped element and transmission line models, is likely to prove useful. If the tip and the sample dimensions are comparable, full electromagnetic field calculations must be implemented. Returning to the case of lumped-element impedance modeling, once the impedance is known from the

measurement, it is possible to use physical models to extract the quantitative parameters of the SUT or DUT. Where possible, we present models generalizable to any experimental case readers may encounter. Below we will demonstrate application of these models to some specific cases for different material parameter categories and show how the parameters of interest can be extracted from the measurements.

### 9.2.2 Near-field, lumped element models

One modeling approach is to represent the tip-sample interaction by a complex, lumped element impedance  $Z_s$ . In the near- or evanescent-field regime, if the tip-sample interaction is lossless, then no net power is transmitted into the sample. The stored reactive energy of the tip-sample interaction may be represented by a reactance  $X_s$  in the lumped element impedance. On the other hand, if the sample or tip is lossy, energy is dissipated. Then the lumped element impedance must include a resistive part,  $R_s$ . The combined lumped element impedance is

$$Z_s = R_s + jX_s \quad , \quad (9.13)$$

where  $j$  is the imaginary unit (As discussed in Chapter 8,  $Z_s$  is in series with the coupling capacitance).  $Z_s$  depends on the tip geometry, the sample properties, and the tip-sample distance. Fig. 9.1 shows an elementary, lumped element circuit representing the tip coupled to the sample:  $C_{cpl}$  is the coupling capacitance,  $C_{str}$  is the stray or parasitic capacitance and  $R_{tip}$  is the probe resistance. Having previously discussed the coupling and the stray capacitance in Chapter 8, here we turn to models of the sample impedance. Several reasonable and practically useful models of the sample impedance were introduced for bulk materials in Reference [9].  $X_s$  and  $R_s$  can be obtained from the integration of the Poynting vector over the whole sample volume. They can be expressed as [9],[10]:

$$X_s = \frac{4\omega}{|I|^2} \int (w_m - w_e) dV \quad (9.14)$$

and

$$R_s = \frac{\omega}{I^2} \int \left( \frac{\sigma}{\omega} |\mathbf{E}|^2 + \epsilon_0 \epsilon'' |\mathbf{E}|^2 + \mu_0 \mu'' |\mathbf{H}|^2 \right) dV \quad , \quad (9.15)$$

where  $I$  is the amplitude of the input current at the tip terminal. The scalar permittivity  $\epsilon_s = \epsilon_0(\epsilon' - j\epsilon'')$  and the permeability  $\mu = \mu_0(\mu' - j\mu'')$ . The variables  $w_m = \frac{\mathbf{B}\mathbf{H}^*}{4}$  and  $w_e = \frac{\mathbf{E}\mathbf{D}^*}{4}$  in Equation (9.14) are magnetic and electric field densities (The asterisk represents complex conjugation of the variable). The three terms in the integrand of Equation (9.15) represent the conductive, magnetic and dielectric losses in the investigated material, respectively.

Figure 9.1. **General circuit models of tip-sample system.** (a) Lumped element circuit model of probe tip coupled to sample. (b) Lumped element circuit model for a magnetic loop probe coupled to sample. Adapted from S.-C Lee, C. P. Vlahacos, B. J. Feenstra, A. Schwartz, D. E. Steinhauer, F. C. Wellstood, and S. M. Anlage, *Appl. Phys. Lett.* **77** (2000) pp. 4404-4406, with permission from AIP Publishing.

Examination of the total circuit impedance in Fig. 9.1(a) leads to the conclusion that maximum sensitivity to  $Z_s$  can be achieved when the coupling impedance is small with respect to  $Z_s$  and the parasitic impedance

is negligible. This can usually be achieved by making the distance between the tip and the sample much smaller than the diameter of the probe tip (e.g. when the tip is in contact with the sample). A more rigorous statement of the near-field condition is:

$$|k|d_{tip} \ll 1; \quad k = \omega(\varepsilon_0\varepsilon_s\mu_0\mu_s)^{1/2} \quad , \quad (9.16)$$

where  $d_{tip}$  is the effective tip diameter that defines the tip-sample interaction area and  $\omega$  is the radial operation frequency of the microscope. Thus, in the near field [9]

$$Z_s \approx \frac{1}{j\omega\varepsilon_0\varepsilon_s d_{tip}} \quad (9.17)$$

and the lumped element model for a lossy bulk material becomes:

$$Z_s = \frac{\tan\delta}{\omega\varepsilon_0\varepsilon' d_{tip}} - j\frac{1}{\omega\varepsilon_0\varepsilon' d_{tip}} \quad . \quad (9.18)$$

Equation (9.18) can be modified for different classes of materials.

For example, in a low loss dielectric material with loss tangent  $\tan\delta \ll 1$ , Equation (9.18) can be further simplified by neglecting the first term. For a normal metal, Equation (9.18) simplifies to

$$Z_s = \frac{1}{d_{tip}\sigma} \quad , \quad (9.19)$$

which is simply the DC resistance of the interaction volume. For bulk semiconductors free of native oxides,  $R_s$  and  $X_s$  are of the same order and the sample impedance can be expressed as

$$Z_s = \frac{1}{d_{tip}\sigma + j\omega\varepsilon_0\varepsilon' d_{tip}} \quad , \quad (9.20)$$

where  $\sigma$  is the conductivity of the semiconductor. Alternatively, the dielectric properties of semiconductors and other materials can be represented by a plasma-like Lorentz-Drude permittivity [4]

$$\varepsilon_p = \varepsilon' - \frac{\omega_p^2}{\omega(\omega + j\nu)} \quad , \quad (9.21)$$

where  $\omega_p^2 = \frac{e^2 N \nu}{\varepsilon_0 m_{eff}}$  is the plasma frequency,  $\nu$  is the collision frequency,  $e$  is the charge,  $m_{eff}$  the effective mass of the carrier and  $N$  is the concentration. Note that in these expressions, a harmonic  $\exp(j\omega t)$  time dependence is assumed. The impedance is then obtained by inserting this permittivity into Equation (9.17) in place of  $\varepsilon_s$ .

Inductive loop probes provide an effective approach for imaging magnetic materials, albeit with poorer resolution than sharp tip probes. A circuit model of a loop probe is illustrated in Fig. 9.1(b). In this case, the tip sample-impedance can be expressed as [11]

$$Z_s = \frac{\omega^2 M^2}{GZ_{surf} + j\omega L_1} \quad , \quad (9.22)$$

where  $G$  is the geometric factor,  $Z_{surf}$  the complex surface impedance,  $M$  is the mutual tip sample inductance and  $L_1$  is the effective inductance of the sample.

For a scanning-tunneling-microscope-based, resonant NSMM, a hybrid approach that combines lumped elements and transmission lines is used. Specifically, a transmission line is used to model the transmission resonator while a lumped element model is used to characterize the tip-sample interaction [12]. The influence of the sample is modeled as a parallel combination of the tunneling impedance  $Z_t$  and the probe impedance  $Z_p$

$$Z_S = (Z_t Z_p) / (Z_t + Z_p) \quad . \quad (9.23)$$

Recall that in a scanning tunneling microscope, an electrically biased tip is positioned about 1 nm from a conducting sample, giving rise to a tunneling current and corresponding tunneling impedance. If the tunneling impedance is mostly due to dissipative losses in the tunnel junction, this impedance is effectively just a tunneling resistance and  $Z_t \approx Re(Z_t) = R_t$ . In a typical tunneling microscope, in which the tip height  $h$  is on the order of a nanometer, the tunneling resistance can be approximated by

$$R_t(h) = R_0(1 + (h/h_0)^\alpha) \quad . \quad (9.24)$$

The constants  $R_0$ ,  $h_0$  and  $\alpha$  are best obtained from a comparison with measurements. When the probe is raised outside of the tunneling range,  $R_t \rightarrow \infty$  and does not contribute. There can be a significant difference in values of  $R_0$  for AC and DC operation. In the cases when the simple resistance approximation is not valid, the tunneling impedance can be expressed as  $Z_t = R_t(1 + j\omega\tau)$ . The tunneling impedance should have an inductive character and therefore a corresponding characteristic time constant  $\tau$  proportional to  $L_t/R_t$ , where  $L_t$  is the tip inductance.

### 9.2.3 Transmission line models

In some cases, a transmission line model provides a more suitable approach to calculation of  $Z_S$ . Multilayer thin film samples, in which the incident signal may penetrate into subsurface layers, are particularly amenable to this approach. The multilayer material is modeled as a series of cascaded transmission line segments with each segment representing a layer of the material. For example, a transmission line can be used to calculate  $Z_S$  for the specific case of a multilayered solar cell [13], as illustrated in Fig. 9.2. The complex impedance of the multilayer solar cell can be expressed as

$$Z_S \approx Z_n \frac{Z_{sub} + jZ_n\gamma_n t_n}{Z_n + jZ_{sub}\gamma_n t_n} \quad , \quad (9.25)$$

where  $Z_n$ ,  $\gamma_n$ , and  $t_n$  are the impedance, electromagnetic wave propagation constant and thickness of the n-type silicon layer of the stack, respectively. If the impedances of the deepest two layers in Fig. 9.2(a) and 9.2(b) are combined into a single parameter  $Z_{sub}$ , it can be expressed as

$$Z_{sub} \approx jZ_0\gamma_0 t_{sub} \quad . \quad (9.26)$$

$Z_o$  is the impedance of the air,  $\gamma_0$  the propagation constant of the air, and  $t_{sub}$  is the thickness of the substrate. Note that Equations (9.25) and (9.26) are derived under the assumptions that  $\gamma t \ll 1$  and that the effects of the  $\text{TiO}_2$  layer may be neglected.

Figure 9.2. **Model of multiplayer photovoltaic system.** (a) Schematic and (b) equivalent circuit model of a probe tip positioned above a multilayer, photovoltaic structure. Adapted from A. Hovsepyan, A. Babajanyan, T. Sargsyan, H. Melikyan, S. Kim, J. Kim, K Lee and B. Friedman, *J. Appl. Phys.* **106**, (2009) art. no. 114901, with permission from AIP Publishing.

A more general approach that applies to NSMM measurements of layered media accounts for the wavelike nature of the excitation source. In References [14] and [15], the surface impedance of a multilayer planar structure was calculated for the case of vertical and horizontal dipoles. Because most NSMM probes act as vertical electric dipoles, we will summarize that approach. The reader can find the impedance due to horizontal electric dipole and magnetic dipoles in the referenced literature. Consider a sample with  $M$  layers indexed by  $m = 0, 1, \dots, M$  (layer  $m = 0$  corresponds to the free space above the layered half space). The  $m$ -th layer has conductivity  $\sigma_m$ , permittivity  $\epsilon_m$  and permeability  $\mu_m$ . The algebraic form of the NSMM reflection coefficient for the vertical electrical dipole over such a multilayer structure is identical to that of the reflection coefficient calculated for a plane wave incident perpendicularly on a planar layered material. This is due to the fact that the field of a dipole over a stratified half space can be regarded as a spectrum of plane waves whose angle of incidence and reflection is determined by a parameter  $\zeta = k_0 \sin(\theta)$ , where  $k_0$  is the free space wave vector and  $\theta$  is the angle of incidence.

The input impedance of the layered material is  $Z_1$ , which can be expressed through recursive equations [14],[15]:

$$Z_1 = K_1(\zeta) \frac{Z_2(\zeta) + K_1(\zeta) \tanh(\beta_1 t_1)}{K_1(\zeta) + Z_2(\zeta) \tanh(\beta_1 t_1)} \quad , \quad (9.27a)$$

$$Z_2 = K_2(\zeta) \frac{Z_3(\zeta) + K_2(\zeta) \tanh(\beta_2 t_2)}{K_2(\zeta) + Z_3(\zeta) \tanh(\beta_2 t_2)} \quad , \quad (9.27b)$$

and

$$Z_m = K_m(\zeta) \frac{Z_{m+1}(\zeta) + K_m(\zeta) \tanh(\beta_m t_m)}{K_m(\zeta) + Z_{m+1}(\zeta) \tanh(\beta_m t_m)} \quad , \quad (9.27c)$$

with

$$Z_M = K_M(\zeta) \quad , \quad (9.28)$$

where  $t_m$  is the thickness of the  $m$ -th layer. The very last layer is assumed to be a half space. The parameters  $B_m$ ,  $Y_m$ , and  $K_m$  are defined as follows:

$$\beta_m(\zeta) = \sqrt{\zeta^2 + \gamma_m^2} \quad , \quad (9.29a)$$

$$\gamma_m^2 = (j\sigma_m \mu_m \omega - \epsilon_m \mu_m \omega^2) \quad , \quad (9.29b)$$

$$K_m(\zeta) = \frac{\beta_m(\zeta)}{\sigma_m + j\omega\varepsilon_m} \quad (9.29c)$$

The generalized reflection coefficient is

$$\Gamma(\zeta) = \frac{K_0(\zeta) - Z_1(\zeta)}{K_0(\zeta) + Z_1(\zeta)} \quad (9.30)$$

This solution is reminiscent of the one-port reflection coefficient derived for a transmission line [4],[14]. When the incident plane wave is perpendicular to the surface,  $\theta = 0$ ,  $\beta_m = \gamma_m$  and  $K_m = Z_m$ . In the limit where the multilayer structure consists of very thin layers, the equations for the impedance and reflection coefficient of the layered medium are reduced to ordinary differential equations of the so-called Riccati form that can be solved as an initial value problem [16].

### 9.3. Resonant cavity models and methods

#### 9.3.1 Resonant-cavity-based, near-field scanning microwave microscopy

Up to now, we have described the interaction of the tip and the sample by use of a sample impedance. Alternatively, we can treat the whole NSMM system as a specialized transmission cavity [17]. Such a treatment of NSMM was first introduced in Reference [18] and many NSMM instruments intended for material characterization rely on an engineered resonant system inserted between a network analyzer and the tip-sample junction [19]-[21]. Some resonant NSMM implementations operate in a linear regime [17], while others operate in a nonlinear regime [22],[23].

In order to understand resonant NSMM measurements, it is necessary to understand how the tip-sample system can be represented by a load on a resonant circuit. There are several lumped element circuit models that represent a resonant circuit connected to the NSMM probe tip. For example, in Reference [24], the coaxial resonator circuit is modeled as a sixth order LCR notch filter, while in Reference [18] the resonator circuit is modeled by a simple series or parallel RLC circuit. Here, we follow the approach of Reference [17], as shown in Fig. 9.3. The equivalent lumped element circuit of a resonator is coupled to a source as well as the tip-sample junction. The junction is represented by a lumped element circuit, as previously introduced in Fig. 9.1. The application of this model depends upon which method is used to measure the reflection coefficient  $\Gamma$  from the NSMM (In some places, the reflection coefficient is alternately referred to as  $S_{11}$  and we will use both notations).

There are two common measurement techniques. In the first technique, the source frequency is swept in a narrow range around the resonance frequency and  $\Gamma$  is measured as a function of frequency for each probe position. In the second technique, at each probe position,  $\Gamma$  is measured at a single, constant frequency chosen to be near, but not equal to the resonant frequency. Each of these techniques has advantages and disadvantages. The former technique provides a richer set of measurement data, but latter is simpler and faster. Thus, the constant frequency technique is the more common approach, particularly in commercial NSMMs.

Figure 9.3. **Equivalent lumped-element circuit model of a resonant, near-field scanning microwave microscope.** The circuit model comprises, from left to right in the figure, the source, resonator, and the tip-sample system. Adapted from C. Gao and X.-D. Xiang, *Rev. Sci. Instrum.* **69** (1998) pp. 3846-3851, with permission from AIP Publishing.

### 9.3.2. Resonant cavity measurements with swept frequency

In resonator-based NSMM measurements, the majority of the microwave energy is concentrated in the resonant structure or cavity. The probe tip is a weakly coupled extension of this cavity and therefore the tip-sample interaction acts as a perturbation of the cavity response. Thus, perturbation theory, which is well established for microwave resonators, can be used. The influence of the perturbation upon the resonator is characterized by a shift of the resonance frequency  $f_r$  and a change in the loss of the cavity that is represented by the quality factor  $Q$ . From perturbation theory, the relative shift in the resonant frequency can be expressed as [4], [25]

$$\frac{\Delta f_r}{f_r} = - \frac{\int ((\mathbf{E}_1 \cdot \mathbf{D}_0 - \mathbf{E}_0 \cdot \mathbf{D}_1) - (\mathbf{H}_1 \cdot \mathbf{B}_0 - \mathbf{H}_0 \cdot \mathbf{B}_1)) dV}{\int (\mathbf{E}_0 \cdot \mathbf{D}_0 - \mathbf{H}_0 \cdot \mathbf{B}_0) dV} \quad , \quad (9.31)$$

where  $\mathbf{D}_i$ ,  $\mathbf{E}_i$ , and  $\mathbf{B}_i$ ,  $\mathbf{H}_i$  are perturbed ( $i = 1$ ) and unperturbed ( $i = 0$ ) electric and magnetic fields and the integration has to be done over the whole volume of the sample. In terms of the scalar permittivity and permeability, this equation can be expressed as

$$\frac{\Delta f_r}{f_r} = \frac{\int (\Delta \epsilon' \mathbf{E}_1 \cdot \mathbf{E}_0 + \Delta \mu' \mathbf{H}_1 \cdot \mathbf{H}_0) dV}{\int (\epsilon_0 \mathbf{E}_0^2 + \mu_0 \mathbf{H}_0^2) dV} \quad . \quad (9.32)$$

The resonator quality factor is given by

$$Q = \frac{\omega W_{st}}{P_{loss}} \quad , \quad (9.33)$$

where  $W_{st}$  is the stored energy in the cavity and  $P_{loss}$  is the loss of the cavity. The change in the quality factor is

$$\Delta \left( \frac{1}{Q} \right) = \frac{\int (\Delta \epsilon'' \mathbf{E}_1 \cdot \mathbf{E}_0 + \Delta \mu'' \mathbf{H}_1 \cdot \mathbf{H}_0) dV}{\int (\epsilon_0 \mathbf{E}_0^2 + \mu_0 \mathbf{H}_0^2) dV} = - \frac{\Delta f_r}{f_r} \tan \delta \quad . \quad (9.34)$$

For some specific cases, it is possible to use a simple, transmission line approach to obtain the frequency and quality factor shifts from  $\Gamma$  [27]. For a resonator of length  $L$ , it is possible to write  $\Gamma$  as [27]

$$\Gamma = \frac{\Gamma_c + \Gamma_t e^{-2\gamma L} - 2\Gamma_c \Gamma_t e^{-\gamma L}}{1 - \Gamma_c \Gamma_t e^{-2\gamma L}} \quad , \quad (9.35)$$

where  $\Gamma_c$  is the cavity coupling reflection coefficient,  $\Gamma_t$  is the reflection coefficient at the tip, and  $\gamma$  is the propagation constant of the transmission line. From Equation (9.35), it follows that if the reflection

coefficient is only weakly dependent on frequency, *i.e.* if  $f_0 \partial |\Gamma_{c,t}| / \partial \omega \ll 1$  and  $f_0 \partial (\arg \Gamma_{c,t}) / \partial \omega \ll 1$ , then [26]

$$\Delta f_r \approx \frac{1}{2\pi} \frac{\sum_i \partial \varphi / \partial c_i}{\partial \varphi / \partial \omega} = \frac{1}{2\pi} f_0 \sum_x \frac{\partial \arg(\Gamma_t)}{\partial c_x} d c_x \quad , \quad (9.36)$$

where  $\varphi = \arg(\Gamma_c \Gamma_t e^{-2\gamma L})$  and  $f_0$  is the unperturbed, fundamental resonance frequency of the resonator. The circuit variable set  $\{c_x\} = \{C_{str}, C_{cpl}, Z_s(C_s, R_s)\}$  is drawn from the equivalent circuit in Fig. 9.3 or other equivalent circuits. The circuit variables are directly related to the change of the resonance frequency in the experiment. If one can neglect the tip resistance  $R_t$ , Equation (9.36) can be simplified to

$$\frac{\Delta f_r}{f_r} \approx -2Z_0 f_0 \sum_i \frac{\partial C_t}{\partial c_i} d c_i \quad . \quad (9.37)$$

$C_t$  is the effective tip capacitance derived from the given lumped element circuit. Under the same assumption, the change of the quality factor can be expressed as [26]

$$\Delta \left( \frac{1}{Q} \right) = \frac{4}{\omega} f_0 Z_0 \Delta G \quad . \quad (9.38)$$

$\Delta G$  is the change in the parallel conductance of the sample (defined by the sample impedance  $Z_s(R_s, C_s)$ ) from Fig. 9.3 and represents the changes in the loss within the sample. Note that  $G_p/\omega$  directly determines the losses in the sample.

The exact forms of the solutions to Equations (9.31), (9.32), and (9.34) depend on the geometry of the system, material properties and boundary conditions. Therefore, we will not include here a derivation of general analytic solutions to those equations in terms of a Green's function or other formulation. Experimentally, the local permittivity and permeability may be determined by use of Equations (9.31), (9.32), and (9.34), as follows. The frequency shift, *i.e.* the left hand side of Equations (9.31) and (9.32), is obtained from measurement of the reflection coefficient during a frequency sweep around the resonance frequency. To obtain the shift, this measurement must be carried out both when the resonator is unperturbed (far from the sample) and when the resonator is loaded (near the sample). The measurement of the frequency shift of the cavity with respect to the unperturbed resonance frequency can be obtained directly.

Obtaining the shift in the cavity quality factor  $\Delta Q$  from the measurements can be confusing. Intuitively, one might assume the quality factor of the resonant cavity is obtained directly from the fitting the observed frequency dependence in the vicinity of the resonant frequency. This is incorrect and therefore we will spend some time to define the correct approach following the procedure described in Reference [28]. Considering the circuit model of the resonant cavity in Fig. 9.3, it is possible to define an external quality factor  $Q_E$  associated with the power dissipation due to coupling of the cavity to the external circuitry (e.g. the iris in waveguide cavities). It is also possible to define a quality factor  $Q_V$  associated with the dissipation within the cavity volume (e.g. the combined cavity and sample dissipation volumes). The overall  $Q_L$  factor of the cavity then can be expressed as

$$\frac{1}{Q_L} = \frac{1}{Q_E} + \frac{1}{Q_V} \quad . \quad (9.39)$$

It is useful to introduce reduced parameters  $\delta_E = Q_E \Delta_\omega$ ,  $\delta_V = Q_V \Delta_\omega$ , and  $\delta_L = Q_L \Delta_\omega$ , with  $\Delta_\omega = \frac{\omega}{\omega_r} - \frac{\omega_r}{\omega}$ . In addition, by introducing  $\beta = Q_V/Q_E = \frac{(1 \mp S_{11r})}{(1 \pm S_{11r})}$ , where  $S_{11r}$  is the reflection coefficient at resonance frequency, as a coupling coefficient of the cavity, it is possible to relate the reduced parameters to the measured reflection coefficient  $S_{11}(\omega)$  as [28]

$$\delta_V = \pm \sqrt{\frac{(1+\beta)^2 S_{11}^2 - (1-\beta)^2}{1-S_{11}^2}} \quad (9.40)$$

The  $\pm$  sign in Equation (9.40) is determined by sign of  $\Delta_\omega$  which is negative for  $\omega_r < \omega$  and positive for  $\omega_r > \omega$ . The other reduced parameters can be determined from  $\delta_V$  by  $\delta_E = \delta_V/\beta$  and  $\delta_L = \delta_V/(1 + \beta)$ . Plotting the reduced parameters as a function of  $\Delta_\omega$  and obtaining a linear fit yields  $Q_E$ ,  $Q_V$ , and  $Q_L$ . An example of the measured frequency dependence of the reflection coefficient and the deduction of the quality factors is shown in Fig. 9.4. Specifically, Fig. 9.4(a) shows the frequency-dependence of the reflection coefficient and Fig. 9.4(b) shows the parameter  $\delta_V$  as a function of  $\Delta_\omega$ . It is possible to use a similar procedure to obtain the quality factor for a transmission cavity in which  $S_{21}$  is measured.

**Figure 9.4. Obtaining the cavity quality factor from resonant, near-field scanning microwave microscope measurements.** (a) A comparison of measured (solid grey line) and calculated (dashed black line) reflection coefficients as a function of frequency. (b) The experimental reduced parameter  $\delta_V$  (solid grey line) is determined from the measured reflection coefficient. A linear fit (dashed black line) to the experimental data provides the quality factor  $Q_V$  associated with the dissipation within the cavity volume. Further, the fitted values of  $\delta_V$  are used to find the calculated reflection coefficient in (a).

NSMM-based measurements of the complex permittivity of bulk materials provide a practical example of material characterization through measurement of the frequency shift and change in the quality factor [29]. We consider specific examples of frequency-swept measurements that reveals a number of issues that are important for quantitative characterization of material properties. A typical experimental configuration of an NSMM resonator is described in Reference [17]. The bulk SUTs studied therein include dielectrics, semiconductors and metals. The experimental data confirmed that the shift of the resonance frequency is most sensitive to the tip-sample coupling capacitance  $C_{cpl}$  and the capacitive contribution to the sample impedance  $Z_s$  (See Fig. 9.3), while the change of the quality factor is most sensitive to the resistive contribution to  $Z_s$  (Although, in general both shifts are functions of  $C_{cpl}$  and the total sample impedance  $Z_s$ ).

In the specific examples of fused silica and silicon, the shift in the resonance frequency and the quality factor were measured by use of frequency-swept measurements at each height in the range from 0.1 to 1000  $\mu\text{m}$  above the sample. The experimental results are shown in Fig. 9.5 where  $\Delta f/f_0$  is plotted against  $Q/Q_0$ . The unperturbed values of  $f_0$  and  $Q_0$  of the unloaded resonator are measured at the height of 1000  $\mu\text{m}$ . As seen in Fig. 9.5, there is a significant, height-dependent frequency shift but little change

in quality factor for the fused silica, as expected for a low loss material. For the silicon, in which the loss is significantly higher, there is a significant change in both the quality factor and the resonant frequency. To extract the material properties from the experimentally observed dependences for dielectric and semiconducting materials, the coupling capacitance can be successfully modeled by the quasi-static image charge method discussed in Chapter 7. The sample properties can be modeled by use of the lumped element approach, as described in Equations (9.16) through (9.19). In this example, when the sample is modeled as a series RLC circuit the input impedance of the resonator is [27]

$$Z_{in} = R_{res}(1 + 2j(Q \Delta f / f_0)) \quad , \quad (9.41)$$

where  $R_{res}$  is the series resistance of the resonator equivalent circuit.

Figure 9.5. **NSMM measurements of silicon and fused silica.** The normalized shift of the resonance frequency is shown as a function of the change in the resonator quality factor for bulk silicon (open circles) and bulk fused silica (open triangles). Fitted curves for a quasistatic model are shown as solid lines for both samples. Reprinted from A. Imtiaz, T. Baldwin, H. T. Nembach, T. M. Wallis and P. Kabos, *Appl. Phys. Lett.* **90** (2007) art. no. 243105, with permission from AIP Publishing.

There are several different ways to visualize height-dependent NSMM measurements, each of which brings out different features. In general, different materials with different complex permittivity values will present different loads to the resonator. Data plotted with  $\Delta f$  as a function of  $Q$ , as in Fig. 9.5 visually distinguish different classes of materials – dielectrics, semiconductors, and metals - based on differences in the loss. By contrast, plotting  $Q$  as a function of height offers little distinction between the respective responses of metal and dielectrics. Finally, a plot of the product  $(\Delta f / f_0) (Q / Q_0)$  versus height highlights the capacitive coupling to the sample load.

A pure quasi-static model of the tip-sample interaction fails for metals. In particular, it is necessary to include a calculation of the near field antenna impedance as it is brought close to a metal surface, as discussed in Chapter 8. The reason for this is that there is non-negligible resistive loss in the antenna (probe tip) as it is brought close to the metal surface.

### 9.3.3. Calibration, uncertainty, and sensitivity

To model and extract the correct material properties, an unknown critical parameter - the effective tip diameter  $d_{Tip}$  - must be obtained. One technique to find  $d_{Tip}$  is via the calibration procedures discussed in Chapter 8. Another possibility is to use a low loss dielectric with known permittivity as a calibration sample. This is essentially a simplified calibration procedure for height-dependent NSMM of bulk materials. To obtain the effective tip diameter from the measured dependence of  $\Delta f$  versus height for the known, low-loss calibration material, one need only fit that data with the single fitting parameter  $d_{Tip}$ .

Another calibration approach is presented in Reference [30], in which the permittivity of a thin film was obtained. The experimental system comprised a loop-coupled cavity operating as a transmission resonator and a probe tip protruding from the bottom of that cavity. The system was calibrated by measuring three reference samples: magnesium oxide, neodymium gallate and yttrium-stabilized zirconia. The permittivity of the reference samples was known from measurements made by use of a split post resonator technique. The transmission coefficient of the cavity resonator  $S_{21}$  was measured both for standard samples as well as the thin film at two frequencies: 1.8 GHz and its third harmonic 4.4 GHz. To reduce statistical error, measurements were made at different positions on the film. After these measurements the film was patterned with a coplanar waveguide to measure its permittivity through a complementary method. The measured transmission coefficients were fitted to the equation [30]

$$S_{21}(f) = S_{21L} + \frac{S_{21}(f_0)}{1+jQ_L\Delta\omega} e^{j\phi}; \Delta\omega = \frac{f^2-f_0^2}{f^2}, \quad (9.42)$$

where  $S_{21L}$  is the non-resonant leakage between the ports. The phase shift  $\phi$  is introduced due to the fact that the measurement ports are physically separated from the coupling loops.  $S_{21}(f_0)$  is the transmission coefficient at resonance. The data can be subsequently processed following the perturbation approach introduced in Equations (9.31) through (9.34).

An analysis of the measurement uncertainty is critical for any quantitative measurements of materials with NSMM. In this case, the total uncertainty was estimated from statistical uncertainties in the measurement of tip diameter  $d_{tip}$ , film thickness  $t$ , calibration constant  $A$  and normalized frequency shift as

$$\sigma(\varepsilon_f) = \left[ \left( \frac{\delta\varepsilon_f}{\delta(d_{tip}/2)} \right)^2 \sigma(d_{tip}/2)^2 + \left( \frac{\delta\varepsilon_f}{\delta t} \right)^2 \sigma(t)^2 + \left( \frac{\delta\varepsilon_f}{\delta A} \right)^2 \sigma(A)^2 + \left( \frac{\delta\varepsilon_f}{\delta(\Delta f/f')} \right)^2 \sigma(\Delta f/f')^2 \right]^{\frac{1}{2}} \quad (9.43)$$

where  $\varepsilon_f$  is the permittivity of the film. The differential terms can be obtained from analytical expressions of the frequency shift derived from models of the tip sample interaction, such as the charge image model [17].

The sensitivity of NSMM for measurement impedances is [23]

$$S_f = \frac{g_s \omega_0}{4\pi} \frac{C_c^2}{C_0(C_c+C_s)^2}, \quad (9.44)$$

where  $g_s = A_{eff}/(\xi_s)$ ,  $A_{eff}$  and corresponds to the effective tip area,  $\xi_s$  is the decay length of the evanescent wave,  $C_c$  is the coupling capacitance,  $C_0$  is the capacitance of the equivalent circuit of the resonator, and  $\omega_0$  is the unloaded, radial resonance frequency. To distinguish between the regions of different permittivity it is necessary to fulfill the condition

$$\frac{\Delta\varepsilon}{\varepsilon} = \left( \frac{V_{n(rms)}}{V_{in}} \right) / (S_f S_r \varepsilon) \quad (9.45)$$

with  $S_r$  defined as [22]

$$S_r = \frac{dS_{11}}{d\omega} \approx \frac{Q'}{\omega'_0} \left(1 - \frac{\Delta\omega}{\omega'_0}\right); \Delta\omega = \omega - \omega'_0 \quad . \quad (9.46)$$

$Q'$  and  $\omega'_0$  are the perturbed quality factor and resonance frequency of the resonator due to tip-sample interaction,  $V_{n(rms)} = \sqrt{4k_B TBR}$  is the rms value of the noise voltage generated by resistance  $R$  at temperature  $T$ ,  $k_B$  is Boltzmann constant,  $B$  is the bandwidth of the system, and  $V_{in}$  is the probe input voltage.

#### 9.3.4 Resonant cavity measurements of semiconductors

Semiconductors are foundational for nanoelectronic applications. As the dimensions of semiconductors are scaled to the nanometer range, important questions arise about the applicability of standard semiconductor device theories at these scales. Moreover, such scaled systems are inherently more sensitive to the effects of interfaces and defects. Thus, scanning probe techniques are vital experimental tools for spatially-resolved characterization of these materials. NSMM is but one of many different scanning probe techniques used for the local, nanoscale characterization of semiconducting materials [32], as we will discuss further in Chapter 11.

When a metal NSMM probe tip is in contact with a native or deposited oxide layer on a semiconductor SUT, the tip-sample interface may be treated as a metal-oxide-semiconductor (MOS) system. In order to model the MOS system, a number of modifications must be made to the model shown in Fig. 9.3. For the tip sample assembly, a nanoscale, parallel plate MOS capacitor with effective tip diameter can be used in most cases as a first approximation. As the tip is in a contact with the surface of the sample, there is no need to model the coupling capacitance separately from the sample response. In contact mode, the field is concentrated under the tip and the stray capacitance can be incorporated into the effective tip diameter. This simplifies the sample model, e.g., to a series connection of the oxide and sample capacitances [24]. To further simplify the model, charges at the oxide-semiconductor interface may be neglected. It is important to remember that any 50 Ohm shunt resistor that is sometimes present in commercial system configurations has to be included in the model.

Experimentally, a DC bias  $V_{tip}$  is often applied to the probe tip and varied systematically throughout the measurements. In the case of silicon samples, it has been shown that the sample response under such a varying tip bias can be effectively modeled by use of standard MOS theories [33]. As  $V_{tip}$  is varied, the resonant circuit is perturbed due to changes in the depletion within the semiconductor, resulting in a change in the reflection coefficient measured by the NSMM. If a small, low frequency voltage is added to  $V_{tip}$ , then the derivative  $dS_{11}/dV_{tip}$  may be measured simultaneously by use of a lockin technique. Just as macroscopic capacitance-voltage curves provide an avenue to measure dopant concentration in semiconductors, local, tip-bias-dependent NSMM measurements provide a way to calibrate the local dopant concentration and quantify their distribution throughout the sample [32].

This requires a calibration sample with regions of known dopant concentration  $N_A$ . An ideal calibration sample has a flat surface with no significant topographic variation such that any changes in the measured

reflection coefficient are due to materials contrast. One particular implementation, to which we will refer below, comprises a series of regions of variably-doped silicon, each with a different dopant concentration. Each region is a 1.5  $\mu\text{m}$  – wide strip, such that the materials contrast appears as a series of parallel stripes.

**Figure 9.6 Dependence of NSMM reflection coefficient and sample capacitance as a function of tip bias voltage.** Calculated (a)  $S_{11}$  and (b) sample capacitance as a function of tip bias at 18 GHz for p-doped silicon for at five doping levels: (1)  $N_A = 1 \times 10^{15} \text{ cm}^{-3}$ , (2)  $N_A = 1 \times 10^{16} \text{ cm}^{-3}$ , (3)  $N_A = 1 \times 10^{17} \text{ cm}^{-3}$ , (4)  $N_A = 1 \times 10^{18} \text{ cm}^{-3}$ , (5)  $N_A = 1 \times 10^{19} \text{ cm}^{-3}$ . An effective tip area of 30 x 30 nm and 1 nm native oxide thickness are assumed. Reprinted from J. Smoliner, H. P. Huber, M. Hochleitner, M. Moertelmaier, and F. Kienberger, *J. Appl. Phys.* **108** (2010) art. no. 064315, with permission from AIP Publishing.

Tip-bias-dependent measurements of such a calibration sample must first be converted from an  $S_{11}$  measurement into a measurement of the sample capacitance  $C_{\text{sample}}$  (or  $dS_{11}/dV_{\text{tip}}$ ) into  $dC_{\text{sample}}/dV_{\text{tip}}$ ). The resulting capacitance-voltage measurement curves may then be compared to corresponding simulated curves for selected values of  $N_A$ , which provides an approach for converting  $S_{11}$  measurements into dopant concentrations measurements. Examples of tip-bias-dependent  $S_{11}$  measurements and  $C_{\text{sample}}$  calculations for various dopant concentrations in p-doped silicon are shown in Fig. 9.6. In order to accurately simulate the MOS system and extract accurate dopant concentration from the measurements, additional parameters such as oxide thickness and the effective tip diameter have to be known [32]. The simulation package FASTC2D [34], [35] incorporates the relevant parameters into a quasi-static, three-dimensional model of a MOS capacitor formed between tip and the oxidized semiconductor surface, leading to rapid conversion of  $dC_{\text{sample}}/dV_{\text{tip}}$  measurements to dopant profiles. An example of calibrated dopant profiling is shown in Fig. 9.7 [36]. Further details of dopant profiling in semiconductors, including calibration samples, measurement techniques, and modeling, are discussed in Chapter 11.

**Figure 9.7. Dopant profiling with NSMM.** (a) Dopant calibration curves showing the dC/dV amplitude with respect to the dopant concentration for n-doped (black circles) and p-doped (grey squares) reference samples. Lines have been added to guide the eye. The data were obtained from dC/dV images by averaging the dC/dV amplitude at various regions of known doping concentrations. (b) dC/dV image of a p-doped test sample with four different doping densities:  $6 \times 10^{15}$  (region 1),  $8 \times 10^{16}$  (region 2),  $1 \times 10^{17}$  (region 3), and  $1 \times 10^{19}$  atoms/cm<sup>3</sup> (region 4). Regions 2 and 3 are 300 nm wide. (c) Average cross-section of the image shown in (b). Adapted from H. P. Huber, et. al., *J. Appl. Phys.* **111** (2012) art. no. 014301, with permission from AIP Publishing.

Another critical parameter that influences NSMM results is the operating frequency. Naively, one might assume there is no significant difference to be expected in the frequency range commonly used by NSMMs (1 GHz to 50 GHz). In practice, the selection of the operating frequency may have a significant impact on the experimental results. This is because the measured response in many semiconducting materials is frequency dependent. For example, frequency-dependent materials contrast due to change of sheet

resistance was observed in boron-doped silicon [37]. A more systematic investigation of the influence of the frequency was carried out on the “striped” calibration sample described above [32],[38]. In order to compare results at different operating frequencies, a phase shifter is inserted into the microwave signal path between the VNA and the NSMM resonator, as illustrated in Fig. 9.8(a). With  $V_{tip}$  equal to zero, at each operating frequency, the phase shifter is used to tune the reactance of the input impedance such that sample the reflection coefficient has a magnitude of about – 50 dB. In Fig. 9.8(b), the vertical lines in the NSMM image delineate areas of different p-type dopant concentrations. The horizontal, black, dashed lines represent changes in the DC tip bias. The series of DC tip biases is denoted at the right edge of the image. For this image acquired at 5 GHz, there is increased NSMM sensitivity in the stripe with a doping concentration of  $10^{17} \text{ cm}^{-3}$  while the NSMM contrast for the other doping concentrations is suppressed. As the operating frequency is switched to other values - 2.3 GHz, 9.6 GHz, 12.6 GHz and 17.9 GHz – increased sensitivity is observed in different ranges of dopant concentrations. Fig. 9.8 (d) shows a calculation of the frequency-dependent input impedance for a given dopant concentration. The maximum in the input impedance represents an optimal operating frequency or “selection frequency.” Fig. 9.8 (c) shows calculated selection frequencies as a function of the doping concentration. The experimental results are in reasonable agreement with these theoretical predictions and generally support the application of standard MOS theory to such measurements. These measurements underscore the significant potential of NSMM as a broadband tool that reveals physical behavior that can’t be observed via single-frequency measurements, albeit with restrictions that arise from the fact that the experimentally utilized frequencies are constrained by the intrinsic response of the NSMM resonator.

**Figure 9.8. Frequency dependent sensitivity of NSMM.** (a) Schematic of the AFM-based NSMM with the phase shifter. (b) An image of  $d(S_{11})/dV$ , acquired at 5 GHz, illustrating the structure of the sample. Solid white vertical lines delineate the different doped regions: A = bulk silicon, B =  $10^{16} \text{ cm}^{-3}$ , C =  $10^{17} \text{ cm}^{-3}$ , D =  $10^{18} \text{ cm}^{-3}$ , E =  $10^{19} \text{ cm}^{-3}$ , and F =  $10^{20} \text{ cm}^{-3}$ . The dashed black lines demarcate regions of various applied tip bias voltages. (c) Calculated selection frequency vs. doping concentration (solid lines) for 2.3 GHz, 5.0 GHz, 9.6 GHz, 12.6 GHz and 17.9 GHz. The rectangles represent the measured concentrations from the highlighted areas at a given frequency. (d) Calculated input impedance vs. frequency. The operating frequency 12.6 GHz is most sensitive to concentrations near  $10^{17} \text{ cm}^{-3}$ , while 9.6 GHz and 17.9 GHz are most sensitive to  $10^{16} \text{ cm}^{-3}$  and  $10^{18} \text{ cm}^{-3}$ , respectively. Reprinted from A. Imtiaz, T. M. Wallis, S.-H. Lim, H. Tanbakuchi, H.-P. Huber, A. Hornung, P. Hinterdorfer, J. Smoliner, F. Kienberger, and P. Kabos, *J. Appl. Phys.* **111** (2012) art. no. 093727, with permission from AIP Publishing.

The observed, frequency-dependent response of NSMM is attributed to the underlying physics within the sample as described by standard MOS diode theory [33], [39]. From MOS diode theory the space-charge density may be calculated as a function of the surface potential defined with respect to intrinsic Fermi level. Knowing the space charge density, it is possible to solve for the surface charge density  $Q_s(\psi_s)$ , where  $\psi_s$  is the surface potential. Next it is necessary to calculate the depletion layer capacitance  $C_{depl} = \partial Q_s / \partial \psi_s$ , which is a function of the tip-bias voltage. In the NSMM measurements, one has to consider

only high frequency branch of this capacitance. The microscope is sensitive to changes in the series combination of the oxide and  $C_{depl}$  capacitances. In addition, incident microwave power is dissipated in the sample through the surface resistance  $R_{surf}$ , which is given by

$$R_{surf} = \rho_s / \delta_{sd} \quad , \quad (9.47)$$

where  $\rho_s$  is the resistivity of the locally doped region and  $\delta_{sd} = \sqrt{\rho_s / \mu_0 \pi f}$  is the skin depth of the penetrating microwave field. This resistance is in series with the sheet resistance of the semiconductor

$$R_{sh} = \rho_s / d_{eff} \quad , \quad (9.48)$$

where  $d_{eff}$  is an effective length scale corresponding roughly to the distance from the top of the sample to the nearest grounding conductor. This optimal NSMM operating frequency, or “selection frequency,” is inversely proportional to the selection time constant

$$\tau_{sel} = \xi \frac{(R_{surf} + R_{sh})}{C_{tot}} \quad , \quad (9.49)$$

where

$$C_{tot} = \frac{C_{depl} C_{ox}}{C_{depl} + C_{ox}} \quad . \quad (9.50)$$

The parameter  $\xi$  is dimensionless and is proportional to  $\left(\frac{4\delta_{sd}}{d_{tip}}\right)^2$ . Note that NSMM measurements in the frequency range between 1 GHz and 50 GHz of n-doped samples show no frequency dependence. This is attributed to the fact that the mobility of the holes in a p-type sample is about ten times smaller than the mobility of electrons in n-type samples. Thus p-type samples will display a higher resistivity and in turn a higher  $\tau_{sel}$  relative to n-type samples. In order to observe frequency-dependent contrast in an n-type sample, the NSMM operating frequency must be significantly higher than 50 GHz.

### 9.3.5. Nonlinear dielectric microscopy of materials

Another application area for resonant NSMM is the imaging of spontaneous polarization of ferroelectric materials based on measurement of the spatial variation of the nonlinear dielectric constant [40]-[44]. The design, shown in Fig. 9.9, is capable of nanometer resolution. The microscope’s signal path consists of an LC resonator in series with a needle probe. The operating frequency of the probe lies in the range between 1 GHz and 6 GHz. An oscillating electric field

$$v(t) = V \cos(\omega_p t) \quad (9.51)$$

is applied in addition to the applied field between the tip and the back electrode under the sample, resulting in a frequency-modulated signal. The nonlinear response of the sample volume beneath the tip to this field leads to a modulation of the sample capacitance  $\Delta C_s(t)$  that in turn leads to a modulation of the probe oscillating frequency. After demodulation, a lock-in amplifier is used to record the capacitance variation.

Figure 9.9. **Schematic diagram of scanning nonlinear dielectric microscope.** Reprinted from Y. Cho, S. Kazuta, and K. Matsuura, *Appl. Phys. Lett.* **75** (1999) pp.2833-2835, with permission from AIP Publishing.

The voltage-dependent capacitance variation can be quantitatively related to the local, nonlinear dielectric constant as follows. The tip-sample capacitance as a function of the voltage  $v$  can be expanded in a Taylor series

$$C_s(t) = C_{s0} + \left(\frac{dC_s}{dv}\right)v + \frac{1}{2}\left(\frac{d^2C_s}{dv^2}\right)v^2 + \frac{1}{6}\left(\frac{d^3C_s}{dv^3}\right)v^3 + \dots \quad (9.52)$$

The displacement can be expressed as a function of the electric field [44]

$$\mathbf{D} = \mathbf{P}_s + [\boldsymbol{\varepsilon}(2)] \cdot \mathbf{E} + \frac{1}{2}[\boldsymbol{\varepsilon}(3)]: \mathbf{E}^2 + \frac{1}{6}[\boldsymbol{\varepsilon}(4)]: \mathbf{E}^3 + \frac{1}{24}[\boldsymbol{\varepsilon}(5)]: \mathbf{E}^4 + \dots, \quad (9.53)$$

where  $\mathbf{P}_s$  is a spontaneous polarization. The variables  $[\boldsymbol{\varepsilon}(i)]$   $i=2,3,..$  are permittivity tensors. For  $i=2$ , this represents the linear permittivity and is a second rank tensor. For higher values of the index  $i$ , the corresponding tensors of increasing rank represent the nonlinear permittivity. The odd, nonlinear terms in (9.53) are sensitive to polarization direction. The ratio of the change in the capacitance  $\Delta C_s(t) = C_s(t) - C_{s0}$  to the static value of the capacitance can be expressed (for isotropic media) as [44]

$$\frac{\Delta C_s(t)}{C_{s0}} \approx \frac{\varepsilon(3)}{\varepsilon(2)} E_p \cos(\omega_p t) + \frac{1}{4} \frac{\varepsilon(4)}{\varepsilon(2)} E_p^2 \cos(2\omega_p t) + \frac{1}{24} \frac{\varepsilon(5)}{\varepsilon(2)} E_p^3 \cos(3\omega_p t) + \dots \quad (9.54)$$

where  $\omega_p$  is the radial lock-in reference frequency.

An atomic-scale image acquired from the  $\varepsilon(4)$  nonlinear dielectric signal is shown in Fig. 9.10. The well-known arrangement of silicon adatoms in a reconstructed Si(111)-7x7 surface is clearly discernable.

Figure 9.10 **Atomic resolution image obtained by use of nonlinear dielectric microscopy [42].** Topography of a reconstructed Si(111)-7x7 surface obtained from the  $\varepsilon(4)$  signal in scanning nonlinear dielectric microscope. [42] © IOP Publishing. Adapted with permission. All rights reserved.

## 9.4. Measurements of thin films and low dimensional materials

### 9.4.1 Materials for radio-frequency nanoelectronics

Bulk samples provide a useful testbed for establishing the capabilities of NSMM to qualitatively and quantitatively characterize materials, but the ultimate objective is to characterize technologically relevant systems, such as thin films and low dimensional systems. The spatially-resolved measurement of nanomaterials is critical for enabling next generation electronic devices. Materials of interest include thin

films with thicknesses on the same order as other critical dimensions, such as grain size or domain size in ferroelectric or magnetoelectric samples. This category also extends to two dimensional materials where the thickness of the material is a single atomic layer, such as graphene and the transition metal dichalcogenides (TMDs).

While our focus here is on broadband scanning probe microscopy as a tool for quantitative imaging and local spectroscopy of materials, NSMM is but one of many complementary techniques for electromagnetic imaging at the nanoscale [45]. These include free space antenna measurements, resonant cavity approaches, and guided-wave methods, including waveguides, coaxial systems, and microstrip lines. Inevitably, these methods require a clear understanding of the interaction of electromagnetic waves with dielectric materials across macroscopic, mesoscopic, and microscopic length scales [46] as well as an understanding of how materials behave when integrated into devices [47].

#### 9.4.2 Dielectric film characterization

The measurement of thin dielectric films deposited on a dielectric substrate represents an interesting example and a particular challenge, especially if the permittivity of the film is not much different from the permittivity of the substrate [48]. One effective strategy is to measure the ratio of the normalized frequency shift of NSMM resonator loaded with a nonmagnetic, dielectric thin film to the frequency shift with the resonator loaded by the bare substrate alone. This ratio does not depend on the calibration constant of the microscope and is equal to the ratio of the perturbed energies of the resonator. In the context of an imaging system, this strategy is particularly appealing if an image can be obtained that includes regions of the film as well as regions of bare substrate. To obtain the permittivity of the film, it is necessary to determine the relationship between the permittivity and the perturbed energy of the resonator either from an appropriate analytical model or by use of numerical techniques. For example, the numerical value of the permittivity may be obtained by comparing measured value of the normalized frequency shift to the results from simulation, as in [49], by fitting the numerical dependences with functions of the type

$$-\frac{\Delta f_r}{f_0} = A \left( \frac{p_1}{p_2(2g/d_{tip})^{p_3} + p_4(2g/d_{tip}) + 1} \right) + F \quad , \quad (9.55)$$

where parameters  $p_i$  are extracted from the numerical simulations for a range of permittivity,  $d_{tip}$  was introduced earlier, while  $A$  and  $F$  are fitting constants [49]. The value of this approach is limited because the fitting functions are not unique and may have different forms. In addition, the number of fitting parameters is large. A similar method may be used to extract the material losses by measuring the ratio of changes in the quality factor instead of the ratio of changes in the frequency.

#### 9.4.3. Measurements of graphene

Atomically-thin structures are among the most important materials for nanoelectronics. The explosion of research of these materials was triggered by the work of Nobel Prize winners Geim and Novoselov on graphene. Graphene has attracted attention due to its outstanding transport properties as well as new fundamental physics [50]. Since the initial work by Geim and Novoselov, a broader range of atomically-

thin materials has been explored. Heterogeneous stacks of atomically-thin materials, sometimes referred to as van der Waals heterostructures, are of particular interest for nanoelectronics applications [51]. By optimizing the ordering and composition of these layered structures, the dynamical response of these systems may be tuned over a broad frequency range, opening new possibilities for both applications and fundamental study. Due to its broadband capability, subsurface measurement capability and sensitivity to doping levels, NSMM is a potentially useful tool for investigation of the properties of graphene. Early applications of NSMM to graphene [52] focused on mapping local conductivity, but in order to realize the full potential of NSMM for atomically thin materials, it will be necessary to determine if the sensitivity of NSMM is sufficient to characterize an atomically-thin layer at the surface of a heterostructure and, ideally, additional layers buried beneath the surface layer.

In principle, the tip-sample interaction for any two-dimensional material should be modeled as a distributed circuit. However, in many cases the standard simplified lumped element model introduced earlier is appropriate (see Fig. 9.3). It is convenient to visualize the complex admittance  $Y$  of the tip-sample system in a  $\text{Re}(Y)$  vs.  $\text{Im}(Y)$  coordinate system, as is commonly done for spreading resistance data [52]. This representation is similar to well-known Cole-Cole diagrams that consist of a semicircle with the center on the imaginary axis (for admittance). An example is shown in the left panel of Fig. 9.11. The radius of the semicircle is

$$r_{sc} = \frac{C_{cpl}}{2\omega(1+C_{ox}/C_{cpl})} \quad (9.56)$$

and the angular distance

$$\varphi = 2\arctan(\omega(C_{cpl} + C_{ox})R_s) \quad (9.57)$$

where  $C_{ox}$  is the capacitance of the oxide layer and  $C_{cpl}$  is the tip-sample coupling capacitance. For comparison, a visualization of the complex admittance in the complex reflection coefficient plane is shown in the right panel of Fig. 9.11. The reflection coefficient plane representation is a conformal mapping of the admittance plane representation.

**Figure 9.11 Visualization of the complex admittance.** (Left panel)  $Y$ -plane spreading resistance plot. The dots represent a series of logarithmically-scaled spreading resistances. (Right panel) The corresponding spreading resistances plotted in the complex reflection coefficient ( $\Gamma$ ) plane. [52] © IOP Publishing. Reprinted with permission. All rights reserved.

Many early NSMM measurements of low-dimensional materials focused on graphene and an abundance of work has been done to develop corresponding sample models. The relationship between the spreading resistance  $R_s$  of the graphene and the graphene sheet resistance  $R_{\blacksquare}$  is given by [52]

$$R_s = \frac{R_{\blacksquare}}{2\pi} \ln \frac{r_g}{r_t} \quad , \quad (9.58)$$

where  $r_g$  is the inner radius of the ground electrode and  $r_t$  is the radius of the contact area to the graphene sample. In the experimental configuration describe in Reference [52],  $r_g$  is usually large and the exact shape of the graphene patch does not significantly influence the result of Equation (9.58). Investigation of the sheet resistance of graphene layers with different thicknesses led to a simplified resistive model tied to the measurement of the reflection coefficient [53]. An alternative characterization method measures the microwave conductivity of graphene by use of a high-Q resonator [54]. Like many implementations of NSSM, the resonator method measures the shifts in the resonant frequency and the quality factor, therefore the analysis is also applicable to NSMM measurements. First, resonator measurements are made on both the bare substrate and the substrate with graphene layer. The change of the resonator loss due to presence of the graphene can be obtained by taking the difference of the measured quality factors. In turn, this difference can be related to the shift of the resonance frequency due to presence of graphene sheet, the material dimensions and material properties. Application of Equation (9.34) results in [54]

$$\Delta\left(\frac{1}{Q}\right) = \Delta\left(\frac{1}{Q_g}\right) - \Delta\left(\frac{1}{Q_s}\right) = \varepsilon_g'' \frac{\Delta f_s t_g}{(\varepsilon_s' - 1)t_s} , \quad (9.59)$$

where  $t_g$  is the thickness of the graphene layer and  $t_s$  is the thickness of the substrate. Similar notation distinguishes the permittivity of the graphene  $\varepsilon_g$  from that of the substrate  $\varepsilon_s$ . The sheet resistance is related to graphene conductivity by

$$R_s = \frac{1}{\sigma t_g} . \quad (9.60)$$

Given the dependence between the conductivity and imaginary component of the dielectric constant,  $\sigma = 2\pi f_0 \varepsilon_0 \varepsilon_g''$ , the sheet resistance is [54]

$$R_s = \frac{\Delta f_s}{2\pi f_0 \varepsilon_0 \Delta\left(\frac{1}{Q}\right)(\varepsilon_s' - 1)t_s} . \quad (9.61)$$

Returning to the particular case of NSMM, it is useful to introduce a simple model of the impedance of a graphene sheet as well as other, similar two-dimensional materials. In one example [55], the tip-graphene interaction in a NSMM was described by a lumped element model consisting of series connection of oxide capacitance, spreading resistance of graphene, and the capacitance between the substrate and the shield of the probe. Here, we develop a general approach based on a two dimensional electron gas (2DEG) [56],[57]. The 2DEG impedance can be expressed as [57]

$$Z_{2DEG} = R_{2DEG} + j\omega L_k; \quad R_{2DEG} = \frac{m_{eff}}{Ne^2\nu}; \quad L_k = \frac{m_{eff}}{Ne^2} \quad (9.62)$$

where  $R_{2DEG}$  is the 2DEG resistance per square and  $L_k$  is the kinetic inductance. More generally, the impedance for a sample of any thickness is determined by use of the Drude conductivity as [56]

$$Z_{gr} = \frac{g_F + 2a}{N} \frac{1 + j\omega\tau}{\sigma} \quad (9.63)$$

where  $g_F$  and  $a$  are form factors depending on the geometry of the probe,  $N$  is number of layers in the graphene stack,  $\tau$  is scattering time and  $\sigma = \mu n_d e$  is the low frequency Drude two-dimensional conductivity.

In order to develop a general model there is an additional parameter that has to be considered, namely the quantum capacitance. Quantum capacitance was introduced in Reference [58] in connection with two-dimensional electron gases and discussed in Reference [59] as an approach for modeling one-dimensional nanoscale devices. The quantum capacitance is defined as

$$C_Q = \frac{\partial Q}{\partial V_l} \quad , \quad (9.64)$$

where  $V_l$  is a local electrostatic potential. The quantum capacitance is conventionally defined per unit length for one-dimensional systems and per unit area for two-dimensional systems. The quantum capacitance depends critically on the form of the density of states. Below we give a few examples of the density of states and corresponding quantum capacitances.

In general, the density of states (DOS) is given by

$$g(E) = \frac{m_{eff}}{\pi \hbar^2} \nu(E) \quad , \quad (9.65)$$

where  $\nu(E)$  is the number of contributing bands at a given energy. Assuming that  $\nu(E)$  may be approximated by a quadratic dependence on energy  $E$ , the quantum capacitance for a two-dimensional system is [59]

$$C_Q = \frac{vm_{eff}e^2}{2\pi\hbar^2} \left[ 2 - \frac{\sinh(E_G/2kT)}{\cosh\left(\frac{E_G/2 - eV_l}{2kT}\right)\cosh\left(\frac{E_G/2 + eV_l}{2kT}\right)} \right] \quad (9.66)$$

where  $E_G$  is the band gap. For  $E_G = 0$  this reduces to [58]

$$C_Q = \frac{vm_{eff}e^2}{2\pi\hbar^2} \quad (9.67)$$

Alternatively, for undoped, single-layer graphene, a linear density of states may be used. If the density of states has the form [60, 61]

$$g(E) = \frac{g_s g_v}{2\pi(\hbar v_F)^2} |E| \quad (9.68)$$

where  $g_s$  is the spin degeneration and  $g_v$  is the valley parameter, then the quantum capacitance is given by

$$C_Q = \frac{2e^2 kT}{\pi(\hbar v_F)^2} \ln \left[ 2 \left( 1 + \cosh\left(\frac{eV_l}{kT}\right) \right) \right] \quad , \quad (9.69)$$

where  $k$  is the Boltzman constant. Under the condition  $eV_l \gg kT$ , Equation (9.69) simplifies to

$$C_Q \approx e^2 \frac{2eV_l}{\pi(\hbar v_F)^2} = \frac{2e^2}{\hbar v_F \sqrt{\pi}} \sqrt{n} \quad , \quad (9.70)$$

where  $n$  is the carrier concentration and  $e$  is the electron charge.

In the one-dimensional case

$$g(E) = \frac{1}{\pi\hbar^2} \nu(E) \sqrt{\frac{2m_{eff}}{E}} \quad (9.71)$$

and the calculation of the quantum capacitance is more complicated. Under special conditions, if  $\nu$  can be considered constant and the DOS can be approximated as

$$g(E) = \frac{\nu}{\hbar v_F} \quad , \quad (9.72)$$

where  $v_F$  is the Fermi velocity, then the one-dimensional quantum capacitance simplifies to

$$C_Q = \frac{2\nu e^2}{\hbar v_F} \quad . \quad (9.73)$$

Experimentally, the local quantum capacitance of graphene or other low dimensional system can be obtained by use of scanning probe microscopy and spectroscopy [62]. Although such measurements have historically been performed with scanning capacitance microscopes, they can also be performed with NSMM. The NSMM tip is positioned near the sample and the reflection coefficient is measured as a function of the tip bias voltage. As needed, a small AC signal may be added to the DC bias to facilitate a more sensitive spectroscopic measurement by use of a lock-in technique.

Consider such a spectroscopic measurement of a mechanically exfoliated graphene flake supported by a SiO<sub>2</sub> layer grown on a Si substrate. Spectroscopic measurements are taken at tip positions above the graphene flake as well as above the bare SiO<sub>2</sub>. The ratio of the reflection coefficient measured with the tip positioned over the graphene to that measured with the tip positioned over the oxide is calculated. Once again, the system consisting of the probe tip over the oxide and Si substrate can be reasonably modeled as a MOS structure, but the model must be modified such that the quantum capacitance is in series with the MOS impedance. The quantum capacitance per unit area  $C_Q$  may then be related to the oxide capacitance per unit area  $C_{ox}$  by

$$C_Q = C_{ox} \frac{V_b}{\Delta V_{gr}} \quad (9.74)$$

where  $V_b$  is the bias voltage and  $\Delta V_{gr}$  is the potential drop across the thickness of the graphene within the effective probe area. The local potential in graphene is dependent on the charge density around the contact and can be expressed as [62]

$$V_{gr}(r) = \frac{\sqrt{\pi}\hbar v_F}{e} \sqrt{|n(r)|} \quad . \quad (9.75)$$

The potential drop within the effective probe area is then obtained by integrating the potential over the effective tip area. The charge density distribution  $n(r)$  depends on the geometry and structure of the measured system and must be calculated either numerically or analytically.

#### 9.4.4. Measurements of transition metal dichalcogenides

Let's turn now from the case of exfoliated graphene to the case of two-dimensional semiconductors, including transition metal dichalcogenides (TMDs). Electrical properties of several TMDs, including metallic and semiconducting systems, are shown in Table 1 [63]. Other two-dimensional semiconductor materials include silicene, phosphorene, and hexagonal boron nitride. Unlike graphene, semiconducting TMDs have a bandgap and are thus suitable for transistor applications.

Table 9.1. **Properties of transition metal dichalcogenides.** Single-layer (1L) and bulk band gaps are listed for the semiconducting materials. Reprinted by permission from Macmillan Publishers Ltd: Nature Nanotechnology. Q. Hua Wang, K. Kalantar-Zadeh, A. Kis, J. N. Coleman and M. S. Strano, *Nature Nanotechnology* **7** (2012) pp. 699-712. Copyright 2012.

	-S <sub>2</sub>	Ref.	-Se <sub>2</sub>	Ref.	-Te <sub>2</sub>	Ref.
	Electronic Characteristics		Electronic Characteristics		Electronic Characteristics	
<b>Nb</b>	Metal; Superconductor; Charge Density Wave	[67]	Metal; Superconductor; Charge Density Wave	[67],[68]	Metal	[72]
<b>Ta</b>	Metal; Superconducting; Charge Density Wave	[67],[68]	Metal; Superconducting; Charge Density Wave	[67],[68]	Metal	[72]
<b>Mo</b>	Semiconductor 1L: 1.8 eV Bulk: 1.2 eV	[69],[70]	Semiconductor 1L: 1.5 eV Bulk: 1.1 eV	[71],[70]	Semiconductor 1L: 1.1 eV Bulk: 1.0 eV	[71],[73]
<b>W</b>	Semiconductor 1L: 1.9 eV - 2.1 eV Bulk: 1.2 eV	[66],[71],[70]	Semiconductor 1L: 1.7 eV Bulk: 1.2 eV	[72],[70]	Semiconductor 1L: 1.1 eV	[72]

Representative TMD materials MoS<sub>2</sub> and WSe<sub>2</sub> have been investigated by NSMM [64], revealing that the sensitivity of NSMM is sufficient to image monolayer semiconducting materials and perform quantitative spectroscopy on them. The signal-to-noise ratio was found to be dependent on the polarity of the tip bias. Fig. 9.12(a) shows NSMM images of a mechanically exfoliated, few-layer W<sub>1-x</sub>Nb<sub>x</sub>Se<sub>2</sub> patch on a SiO<sub>2</sub>/Si substrate while Fig. 9.12(b) shows NSMM images of a single layer MoS<sub>2</sub>. To acquire these images a lock-in technique was used to obtain the real and imaginary parts of the derivative of the reflection coefficient ( $S_R' = \text{Re}(dS_{11}/dV_{tip})$ ,  $S_C' = \text{Im}(dS_{11}/dV_{tip})$ ). The images demonstrate that changes in the DC tip bias induce different levels of contrast in the  $S_R'$  image. Further investigation revealed that for a given material, contrast was observed for only one polarity of the tip bias, which was directly correlated with the polarity

of the charge carriers in the material. There is little contrast in the  $S_c'$  images, regardless of tip bias polarity or magnitude.

Figure 9.12. **NSMM images of transition metal dichalcogenides.** AFM topography (i) and NSMM images (ii-v) of (a) an exfoliated few-layer  $W_{1-x}Nb_xSe_2$  sample; (b) and a single layer  $MoS_2$  sample with tip bias as indicated. Reprinted with permission from S. Berweger, et. al., *Nano Letters* **15** (2015) pp. 1122-1127. Copyright 2015, American Chemical Society.

Further insight into the interpretation of the NSMM measurements was gained through finite-element, multiphysics simulation of the NSMM-TMD system. The objective of the simulation process is to connect the simulated parameters with the materials properties of the sample by relating them to the measured, bias-dependent data. While this approach is phenomenological, it provides insight into the underlying physics with the NSMM probe-TMD sample system. In this case, it is useful to understand the relation between the charge carrier density and the bias voltage  $V_{tip}$ . Specifically, the real part of the measured admittance of the TMD materials was modeled as a function of conductivity. The capacitive behavior of the TMDs was captured by modeling the material as a dielectric sheet with the relative permittivity  $\epsilon_r=7$ . If the band edge DOS is approximated by a quadratic function, the relation between the carrier density  $n_q$  and the conductivity of the given material can be expressed as [65],[66]

$$n_q \propto \mp (aV_{tip} - E_0)^3 = \sigma_i \quad (9.76)$$

where the minus sign corresponds to n-type semiconductor (as in  $MoS_2$ ) and the plus sign to the p-doped semiconductor (as in  $WSe_2$ ). The constant  $a$  reflects the scaling between  $E$  and  $V_{tip}$  and  $E_0$  accounts for doping at zero bias *i.e.*, the Fermi level shift. It is important to note that a reasonable guess from existing published data or independent measurements must be used to make a reasonable estimate of the mobility of the carriers, as this parameter also enters the relation between the charge carriers and the conductivity of the material. Based on the comparison of the model with the experimental data, the tip-bias dependent contrast is attributed to changes of the TMD conductivity. Measurements and modeling agree that both  $MoS_2$  and  $WSe_2$  show strong unipolar charge transport that correlates with the polarity-dependent contrast in NSMM images.

In addition to NSMM imaging, local spectroscopy can be performed at any tip position above the investigated sample. Of especial importance is spectroscopy on single-layer regions, which provides local measurements of electronic structure as well as sensitivity to local defects. Examples of local spectroscopic measurements of TMD samples are shown in Fig. 9.13. The predicted spectra of the phenomenological, numerical modeling are in good agreement with the experimental data. In order to fit the capacitive part of the spectra, it was necessary to include the quantum capacitance in series with the geometric, electrostatic capacitance. Interpretation of NSMM measurements of semiconducting, two-dimensional materials is more challenging than the interpretation of NSMM measurements of graphene, requiring not only consideration of the effects of quantum capacitance, but also accurate modeling of the

sample conductivity, as well as a comprehensive model of the probe, two-dimensional material, and supporting substrate.

Figure 9.13. **Local NSMM spectroscopy of transition metal dichalcogenides.** Resistive (a) and capacitive (b) components of the derivative of the reflection coefficient  $S'_{R,C}$ -voltage sweeps taken from single layer locations in Fig. 9.12. The solid lines in (a) are finite-element simulations fit to the resistive part of the measured signal. Solid and dashed lines in (b) are fits to the capacitive part of the signal with and without taking into account the quantum capacitance in series with geometric capacitance (see insert). Reprinted with permission from S. Berweger, et. al., *Nano Letters* **15** (2015) pp. 1122-1127. Copyright 2015, American Chemical Society.

The successful characterization of thin films and low-dimensional materials by use of NSMM suggests that the technique can have a broader impact for characterization not only of any two-dimensional system, but also more complicated, multilayer heterostructures. With the advantage of relatively high penetration depth at microwave frequencies, this technique is of particular importance for investigation of subsurface interfaces and defects on the properties of heterostructures.

## References

- [1] S. R. de Groot and L. G. Suttorp, *Foundations of electrodynamics* (American Elsevier, 1972).
- [2] U. Kaatz, "Techniques for measuring the microwave dielectric properties of materials," *Metrologia* **47** (2010) pp. S91-S113.
- [3] L. D. Landau and E. M. Lifshitz, *Electromagnetic of Continuous Media* (Addison-Wesley, 1960).
- [4] J. D. Jackson, *Classical Electrodynamics*, 3rd Ed. (Wiley, 1999).
- [5] R. Hornreich and S. Shtrikman, *Physical Review* **161** (1967) pp. 506-512.
- [6] G. T. Rado, *Physical Review* **128** (1962) pp. 2546-2556.
- [7] J. Baker-Jarvis and P. Kabos, "Dynamic constitutive relations for polarization and magnetization," *Physical Review E* **64** (2001) art. no. 056127.
- [8] J. Baker-Jarvis, P. Kabos, and C. Holloway, "Nonequilibrium electromagnetics: Local and macroscopic fields and constitutive relationships," *Physical Review E* **70** (2004) art. no. 036615.
- [9] S. M. Anlage, V. V. Talanov, and A. R. Schwartz, "Principles of near field microscopy," in *Scanning Probe Microscopy, vol. 1*, S. Kalinin and A. Gruverman, eds. (Springer, 2007).
- [10] A. N. Reznik and N. V. Yurasova, "Electrodynamics of microwave near field probing: Application to medical diagnostics," *Journal of Applied Physics* **98** (2005) art. no. 114701.
- [11] S.-C Lee, C. P. Vlahacos, B. J. Feenstra, A. Schwartz, D. E. Steinhauer, F. C. Wellstood, and S. M. Anlage, "Magnetic permeability imaging of metals with scanning near-field microwave microscope," *Applied Physics Letters* **77** (2000) pp. 4404-4406.
- [12] A. N. Reznik, "Electromagnetic model for near field microwave microscope with atomic resolution: Determination of tunnel junction impedance," *Applied Physics Letters* **105** (2014) art. no. 083512.
- [13] A. Hovsepyan, A. Babajanyan, T. Sargsyan, H. Melikyan, S. Kim, J. Kim, K Lee and B. Friedman, "Direct imaging of photoconductivity of solar cells by using near-field scanning microwave probe," *Journal of Applied Physics* **106** (2009) art. no. 114901.
- [14] J. R. Wait, *Electromagnetic waves in stratified media*, (Pergamon Press, 1962).
- [15] J. R. Wait, *Wave propagation theory*, (Pergamon Press, 1981).
- [16] W. Ch. Chew, *Waves and fields in inhomogeneous media*, (Van Nostrand Reinhold, 1990).
- [17] C. Gao and X.-D. Xiang, "Quantitative microwave near field microscopy of dielectric properties," *Review of Scientific Instruments* **69** (1998) pp. 3846-3851.
- [18] G. P. Kochanski, "Nonlinear alternating-current tunneling microscopy." *Physical Review Letters* **62** (1989) pp.2285-2288.

- [19] M. Tabib-Azar, D. -P. Su, A. Pohar, S. R. LeClair, G. Pochak, "0.4  $\mu\text{m}$  spatial resolution with 1 GHz ( $\lambda=30\text{cm}$ ) evanescent microwave probe," *Review of Scientific Instruments* **70** (1999) pp. 1725-1729.
- [20] M. Tabib-Azar and S. R. LeClair, "Novel hydrogen sensors using evanescent microwave probes," *Review of Scientific Instruments* **70** (1999) pp. 3707-3713.
- [21] R. A. Kleinsmit, M. K. Kazimierczuk and G. Kozlowski, "Sensitivity and resolution of evanescent microwave microscope," *IEEE Transactions on Microwave Theory and Techniques* **54** (2006) pp. 639-647.
- [22] S. J. Stranick and P. S. Weiss, "A versatile microwave-frequency-compatible scanning tunneling microscope," *Review of Scientific Instruments* **64** (1993) pp. 1232-1234.
- [23] Y. Cho, "Scanning nonlinear dielectric microscope with super high resolution," *Japanese Journal of Applied Physics* **46** (2007) pp. 4428-4434.
- [24] J. Smoliner, H. P. Huber, M. Hochleitner, M. Moertelmaier, and F. Kienberger, "Scanning microwave microscopy/spectroscopy on metal oxide semiconductor systems," *Journal of Applied Physics* **108** (2010) art. no. 064315.
- [25] D. A. Hill, *Electromagnetic field in cavities*, IEEE Press Series on Electromagnetic wave theory, (John Willey & Sons, 2009).
- [26] A. Tselev, S. M. Anlage, Z. Ma and J. Melngailis, "Broadband dielectric microwave microscopy on micron length scales," *Review of Scientific Instruments* **78** (2007) art. no. 044701.
- [27] D. M. Pozar, *Microwave Engineering*, 2<sup>nd</sup> ed., (Willey, 1998).
- [28] K. D. McKinstry and C. E. Patton, "Methods for determination of microwave cavity quality factors from equivalent circuit models," *Review of Scientific Instruments* **60** (1989) pp. 439-443.
- [29] A. Imtiaz, T. Baldwin, H. T. Nembach, T. M. Wallis and P. Kabos, "Near field microscope measurements to characterize bulk material properties," *Applied Physics Letters* **90** (2007) art. no. 243105.
- [30] D. J. Barker, T. J. Jackson, P. M. Suherman, M. S. Gashinova, and M. J. Lancaster, "Uncertainties in the permittivity of thin films extracted from the measurements with near field microwave microscopy calibrated by image charge model," *Measurement Science and Technology* **25** (2014) art. no. 105601.
- [31] R. A. Oliver, "Advances in AFM for the electrical characterization of semiconductors," *Rep. Prog. Phys.* **71** (2008) art. no. 076501.
- [32] H. P. Huber, I. Humer, M. Hochleitner, M. Fenner, M. Moertelmaier, C. Rankl, A. Imtiaz, T. M. Wallis, H. Tanbakuchi, P. Hinterdorfer, P. Kabos, J. Smoliner, J. J. Kopanski, and F. Kienberger, "Calibrated nanoscale dopant profiling using scanning microwave microscope," *Journal of Applied Physics* **111** (2012) art. no. 014301.
- [33] S. M. Sze, *The Physics of Semiconductor Devices*, (Wiley, 1981).
- [34] J. J. Kopanski, J. F. Marchiando, and J. R. Lowney, "Scanning capacitance microscopy applied to two-dimensional dopant profiling of semiconductors," *Mater. Sci. Eng. B-Solid State Mater. Adv. Tech.* **44** (1997) pp. 46-51.

- [35] J. F. Marchiando, J. J. Kopanski, and J. R. Lowney, "Model database for determining dopant profiles from scanning capacitance microscope measurements," *Journal of Vacuum Science and Technology B* **16** (1998) pp. 463-470.
- [36] J. Smoliner, B. Basnar, S. Golka, E. Gornik, B. Löffler, M. Schatzmayr, and H. Enichlmair, "Mechanism of bias-dependent contrast in scanning-capacitance microscopy images," *Applied Physics Letters* **79** (2001) pp. 3182-3184.
- [37] A. Imtiaz, S. M. Anlage, J. D. Barry and J. Melngailis, "Nanometer-scale material contrast imaging with a near-field microwave microscope," *Applied Physics Letters* **90** (2007) art. no. 143106.
- [38] A. Imtiaz, T. M. Wallis, S.-H. Lim, H. Tanbakuchi, H.-P. Huber, A. Hornung, P. Hinterdorfer, J. Smoliner, F. Kienberger, and P. Kabos, "Frequency selective contrast on variable doped p-type silicon with a scanning microwave microscope," *Journal of Applied Physics* **111** (2012) art. no. 093727.
- [39] E. H. Nicollian and J. R. Brews, *MOS (Metal Oxide Semiconductor) Physics and Technology* (Wiley, 1982).
- [40] Y. Cho, A. Kiriwara, T. Saeki, "Scanning nonlinear dielectric microscope," *Review of Scientific Instruments* **67** (1996) pp.2297-2303.
- [41] Y. Cho, S. Kazuta, and K. Matsuura, "Scanning nonlinear dielectric microscopy with nanometer resolution," *Applied Physics Letters* **75** (1999) pp.2833-2835.
- [42] R. Hirose, K. Ohara, and Y. Cho, "Observation of the Si(111) 7x7 atomic structure using noncontact scanning nonlinear dielectric microscopy," *Nanotechnology* **18** (2007) art. no. 084014.
- [43] K. Tanaka, Y. Kurihashi, T. Uda, Y. Daimon, N. Odagawa, R. Hirose, Y. Hiranaga, and Y. Cho, "Scanning nonlinear dielectric microscopy nanp-science and technology for next generation high density ferroelectric data storage," *Japanese Journal of Applied Physics* **47** (2008) pp. 3311-3325.
- [44] Y. Cho, "Scanning nonlinear dielectric microscopy," *Journal of Materials Research* **26** (2011) pp.2007-2016.
- [45] D. A. Bonnel, D. N. Basov, M. Bode, U. Diebold, S. V. Kalinin, V. Madhavan, L. Novotny, M. Salmeron, U. D. Schwartz, P. S. Weiss, "Imaging physical phenomena with local probes: From electrons to photons," *Reviews of Modern Physics* **84** (2012) pp.1343-1381.
- [46] J. Baker-Jarvis and S. Kim, "The Interaction of Radio-Frequency Fields With Dielectric Materials at Macroscopic to Mesoscopic Scales," *Journal of Research of the National Institute of Standards and Technology* **117** (2012) pp. 1-60.
- [47] P. Quéffelec, M. Le Floch, and P. Gelin, "Broad-Band Characterization of Magnetic and Dielectric Thin Films Using a Microstrip Line," *IEEE Transactions on Instrumentation and Measurement* **47** (1998) pp.956-963.
- [48] S. Huang, H. M. Christen, and M. E. Reeves, "Parameter-free extraction of Thin-Film Dielectric Constants from Scanning Near Field Microwave Microscope Measurements," arXiv:00909.3579v1 [cond-mat.sci] (2009).
- [49] J. H. Lee, S. Hyun, and K. Char, "Quantitative analysis of scanning microwave microscopy on dielectric thin film by finite element calculation," *Review of Scientific Instruments* **72** (2001) pp. 1425-1434.
- [50] G. Fiori, F. Bonaccorso, G. Iannaccone, T. Palacios, D. Neumaier, A. Seabaugh, S. K. Banerjee and L. Colombo, "Electronics based on two-dimensional materials," *Nature Nanotechnology* **9** (2014) pp.768-779.

- [51] A. K. Geim and I. V. Grigorieva, "Van der Waals heterostructures," *Nature* **499** (2013) pp. 419-425.
- [52] A. Tselev, N. V. Lavrik, I. Vlassioux, D. P. Briggs, M. Rutgers, R. Proksch and S. V. Kalinin, "Near-field microwave scanning probe imaging of conductivity inhomogeneities in CVD graphene," *Nanotechnology* **23** (2012) art. no. 385706.
- [53] T. Monti, A. Di Donato, D. Mencarelli, G. Venanzoni, A. Morini, and M. Farina, "Near-Field Microwave Investigation of Electrical Properties of Graphene-ITO Electrodes for LED Applications," *Journal of Display Technology* **9** (2013) pp.504-510.
- [54] L. Hao, J. Gallop, S. Goniszewski, O. Shaforost, N. Klein, and R. Yakimova, "Non-contact method for measurement of microwave conductivity of graphene," *Applied Physics Letters* **103** (2013) art. no. 123103.
- [55] A. Tselev, V. K. Sangwan, D. Jariwala, T. Marks, L. J. Lauhon, M. C. Hersam, and S. V. Kalinin, "Near field microwave microscopy of high-k oxides grown on graphene with an organic seed layer," *Applied Physics Letters* **103** (2013) art. no. 243105.
- [56] V. V. Talanov, C. Del Barga, L. Wickey, I. Kalichava, E. Gonzales, E. A. Shaner, A. V. Gin, and N. G. Kalugin, "Few-Layer Graphene Characterization by Near-Field Scanning Microwave Microscopy," *ACS Nano* **4** (2010) pp. 3831–3838.
- [57] Kang, S.; Burke, P. J.; Pfeiffer, L. N.; West, K. W. AC Ballistic, "Transport in a Two-Dimensional Electron Gas Measured in GaAs/AlGaAs Heterostructures." *Physical Review B* **72** (2005) art. no. 165312.
- [58] S. Luryi, "Quantum capacitance devices," *Applied Physics Letters* **52** (1988) pp. 501-503.
- [59] D. L. John, L. C. Castro, and D. L. Pulfrey, "Quantum capacitance in nanoscale device modeling," *Journal of Applied Physics* **96** (2004) pp. 5180-5184.
- [60] T. Fang, A. Konar, H. Xing, and D. Jena, "Carrier statistics and quantum capacitance of graphene sheets and ribbons," *Applied Physics Letters* **91** (2007) art. no. 092109.
- [61] J. Xia, F. Chen, J. Li and N. Tao, "Measurement of the quantum capacitance of graphene," *Nature Nanotechnology* **4** (2009) pp.505-509.
- [62] F. Giannazzo, S. Sonde, V. Raineri, and E. Rimini, "Screening Length and Quantum Capacitance in Graphene by Scanning Probe Microscopy," *Nano Letters* **9** (2009) pp.23-29.
- [63] Q. Hua Wang, K. Kalantar-Zadeh, A. Kis, J. N. Coleman and M. S. Strano, "Electronics and optoelectronics of two-dimensional transition metal dichalcogenides," *Nature Nanotechnology* **7** (2012) pp. 699-712.
- [64] S. Berweger, J. C. Weber, J. John, J. M. Velazquez, A. Pieterick, N. A. Sanford, A. V. Davydov, B. Brunshwig, N. S. Lewis, T. M. Wallis, and P. Kabos, "Microwave Near-Field Imaging of Two-Dimensional Semiconductors," *Nano Letters* **15** (2015) pp. 1122-1127.
- [65] E. S. Kadantsev and P. Hawrylak, "Electronic structure of single MoS<sub>2</sub> monolayer" *Solid State Communications* **152** (2012) pp. 909-913.
- [66] A. Kuc, N. Zibouche, and T. Heine, "Influence of quantum confinement on the electronic structure of the transition metal sulfide TS<sub>2</sub>" *Physical Review B* **83** (2011) art. no. 245213.

- [67] A. R. Beal, H. P. Hughes, and W. Y. Liang, "The reflectivity spectra of some group VA transition metal dichalcogenides" *Journal of Physics C* **8** (1975) pp. 4236-4248.
- [68] J. A. Wilson, F. J. Di Salvo, and S. Mahajan, "Charge-density waves and superlattices in the metallic layered transition metal dichalcogenides," *Advances in Physics*. **24** (1975) pp. 117–201.
- [69] K. F. Mak, C. Lee, J. Hone, J. Shan, and T. F. Heinz, "Atomically thin MoS<sub>2</sub>: a new direct-gap semiconductor," *Physical Review Letters* **105** (2010) art. no. 136805.
- [70] K. K. Kam and B. A. Parkinson, "Detailed photocurrent spectroscopy of the semiconducting group-VI transition-metal dichalcogenides," *Journal of Physical Chemistry* **86** (1982) pp. 463–467.
- [71] L. Liu, S. B. Kumar, Y. Ouyang, and J. Guo, "Performance limits of monolayer transition metal dichalcogenide transistors," *IEEE Transactions on Electron Devices* **58** (2011) pp. 3042–3047.
- [72] Y. Ding, Y. Wang, J. Ni, L. Shi, S. Shi, and W. Tang, "First principles study of structural, vibrational and electronic properties of graphene-like MX<sub>2</sub> (M=Mo, Nb, W, Ta; X=S, Se, Te) monolayers," *Physica B: Condensed Matter* **406** (2011) pp. 2254–2260.
- [73] *Gmelin Handbook of Inorganic and Organometallic Chemistry* 8th ed. Vol. B7 (Springer, 1995).

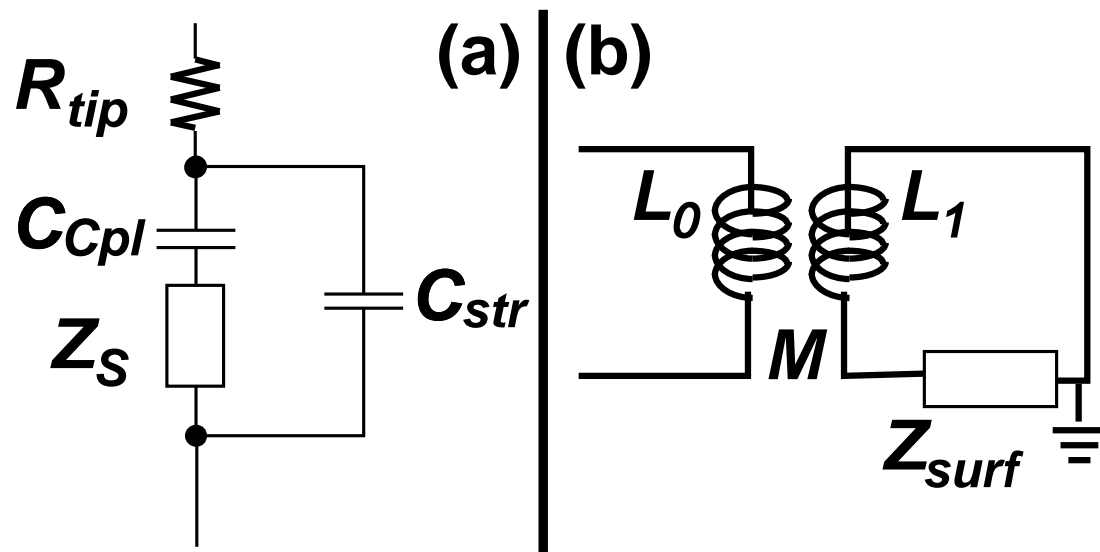
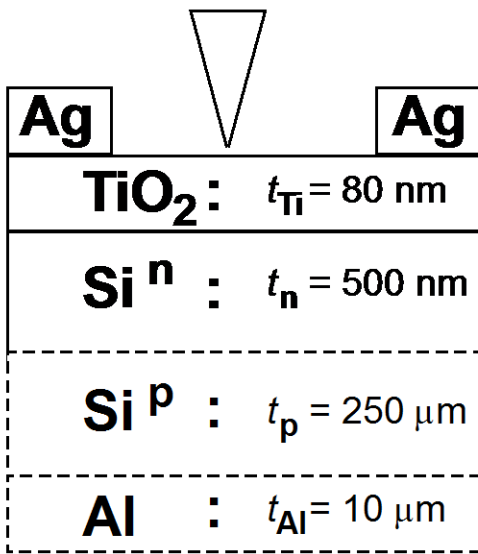


FIGURE 9.1

(a)



(b)

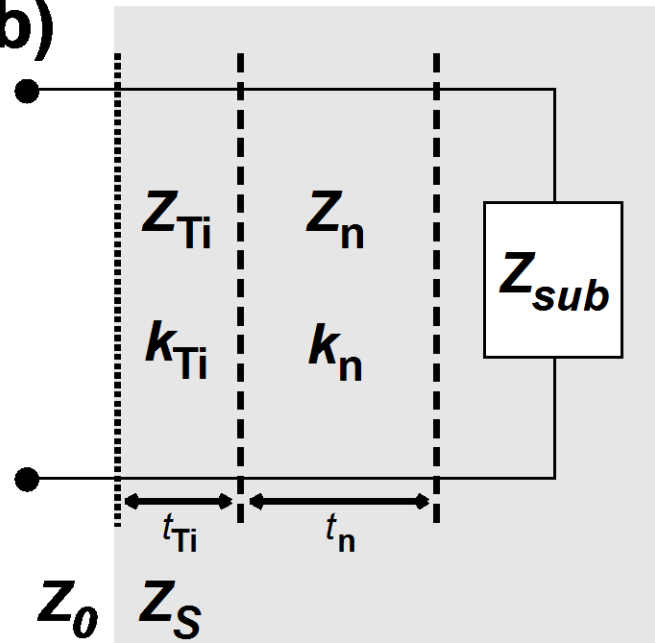


FIGURE 9.2

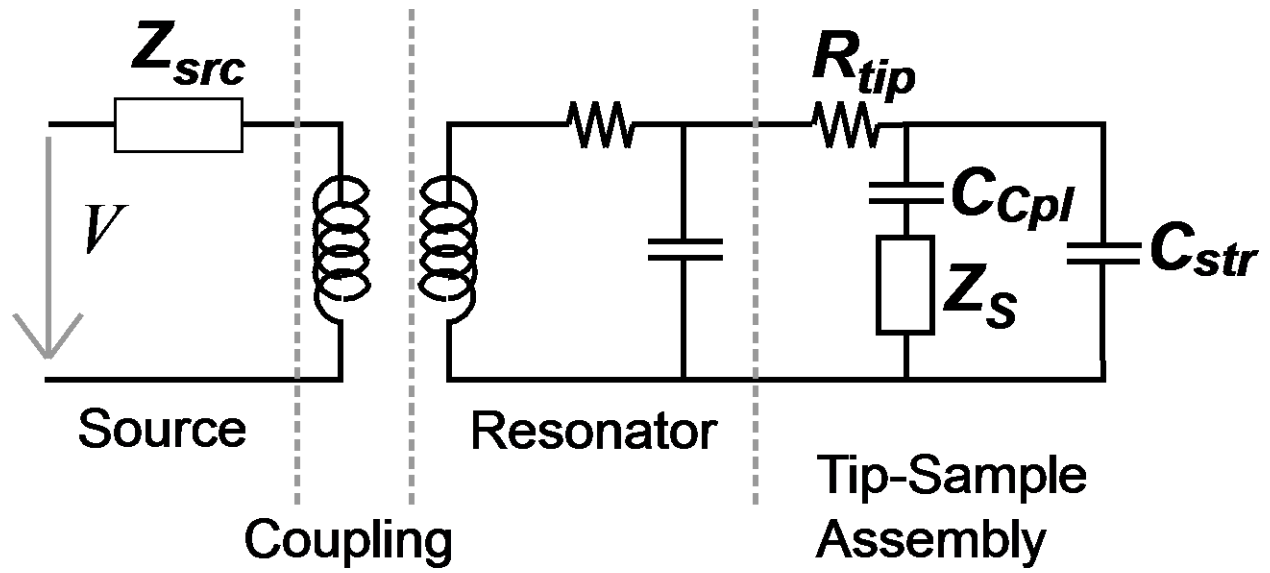


FIGURE 9.3

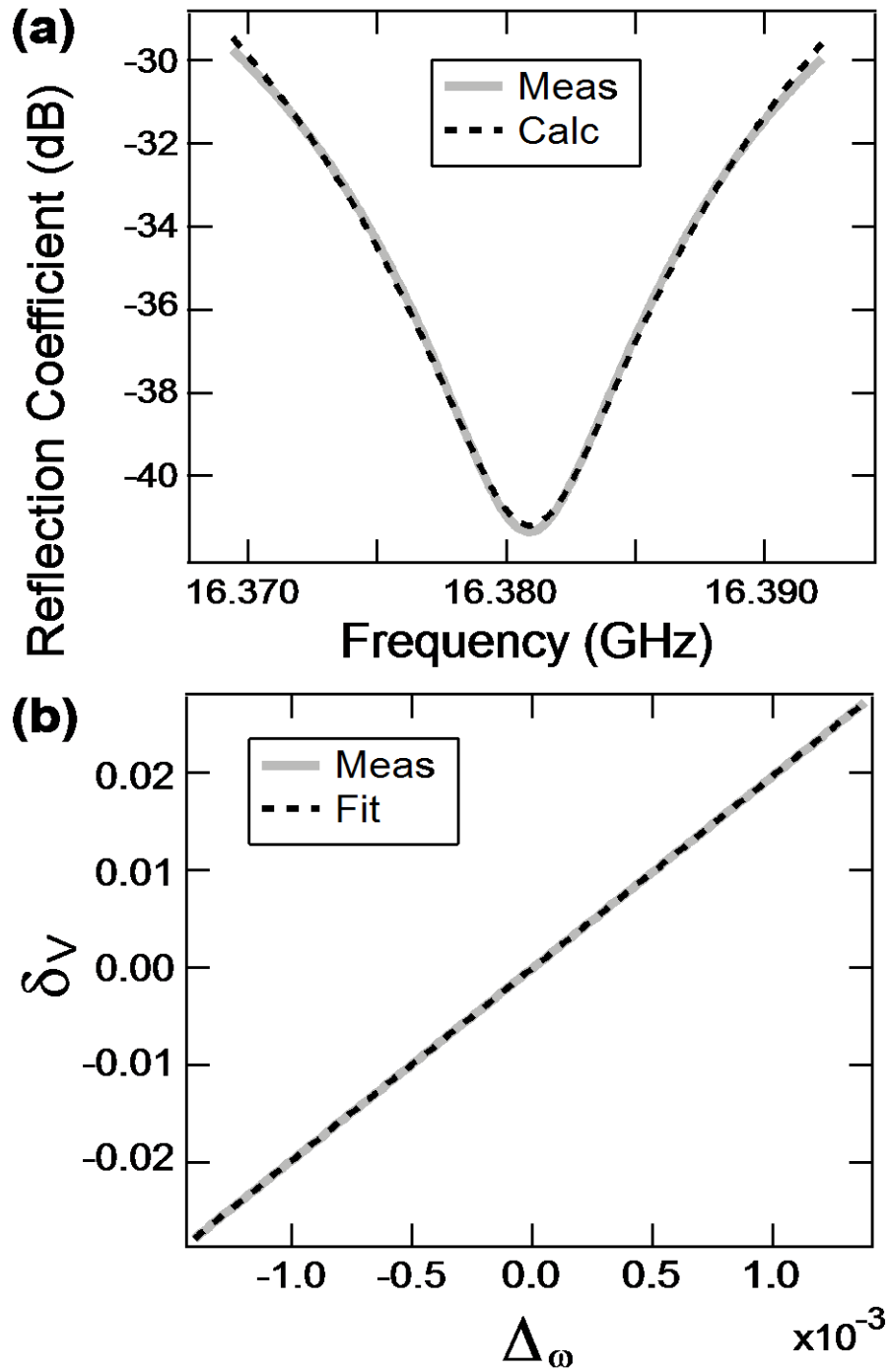


Figure 9.4

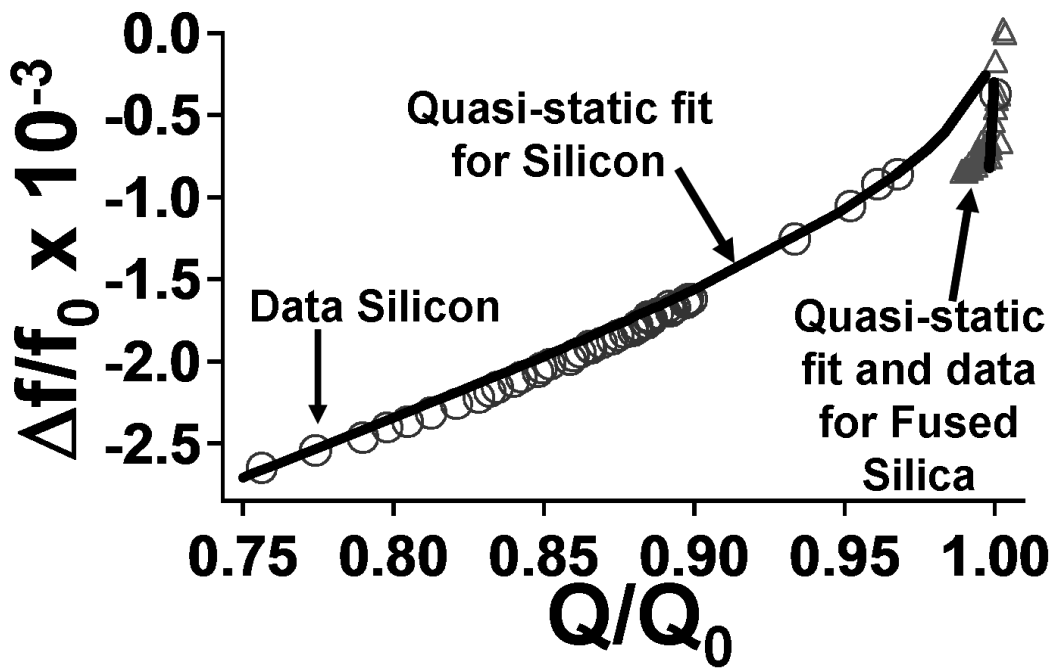


Figure 9.5

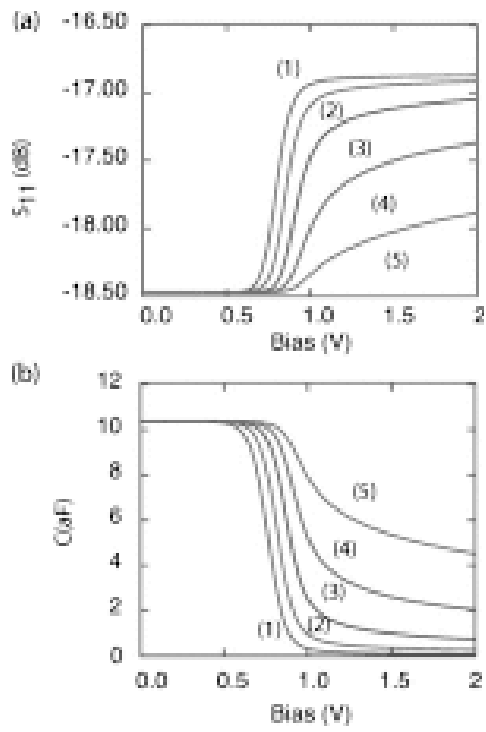
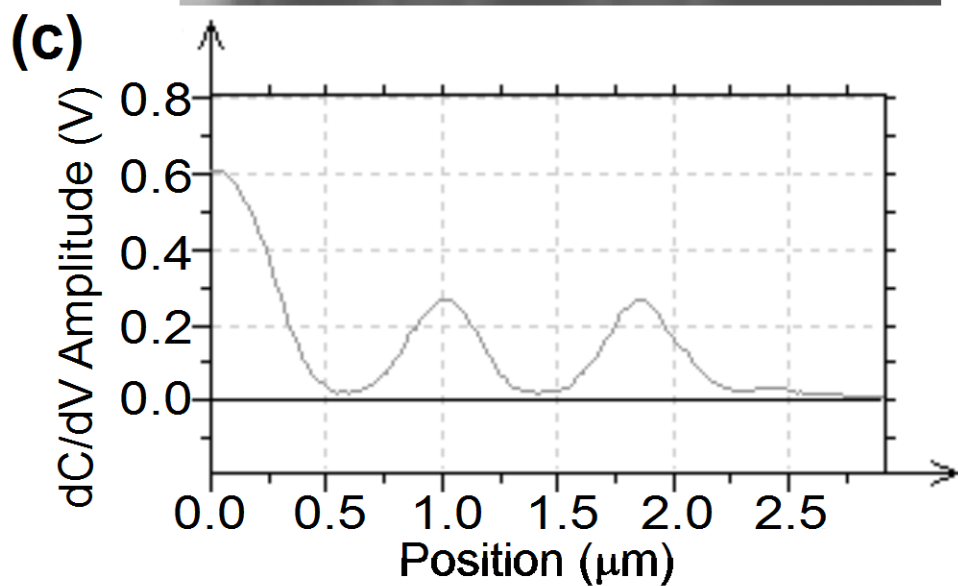
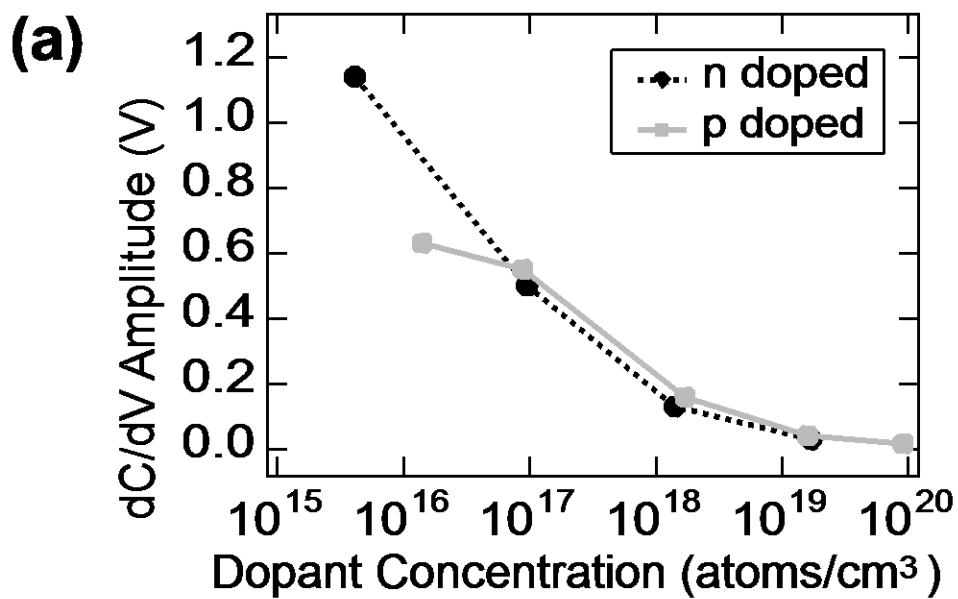


Figure 96



**Figure 9.7**

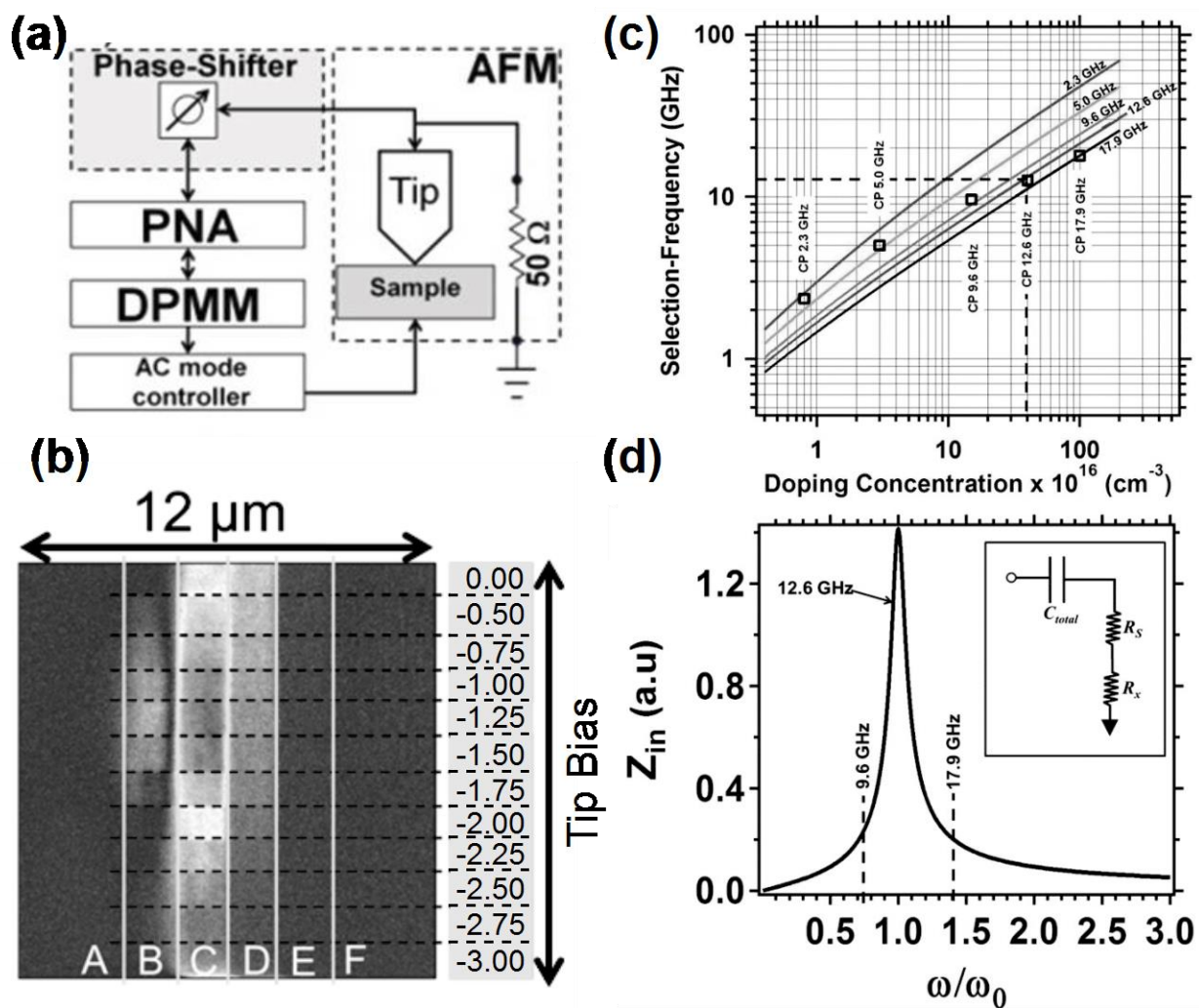


Figure 98

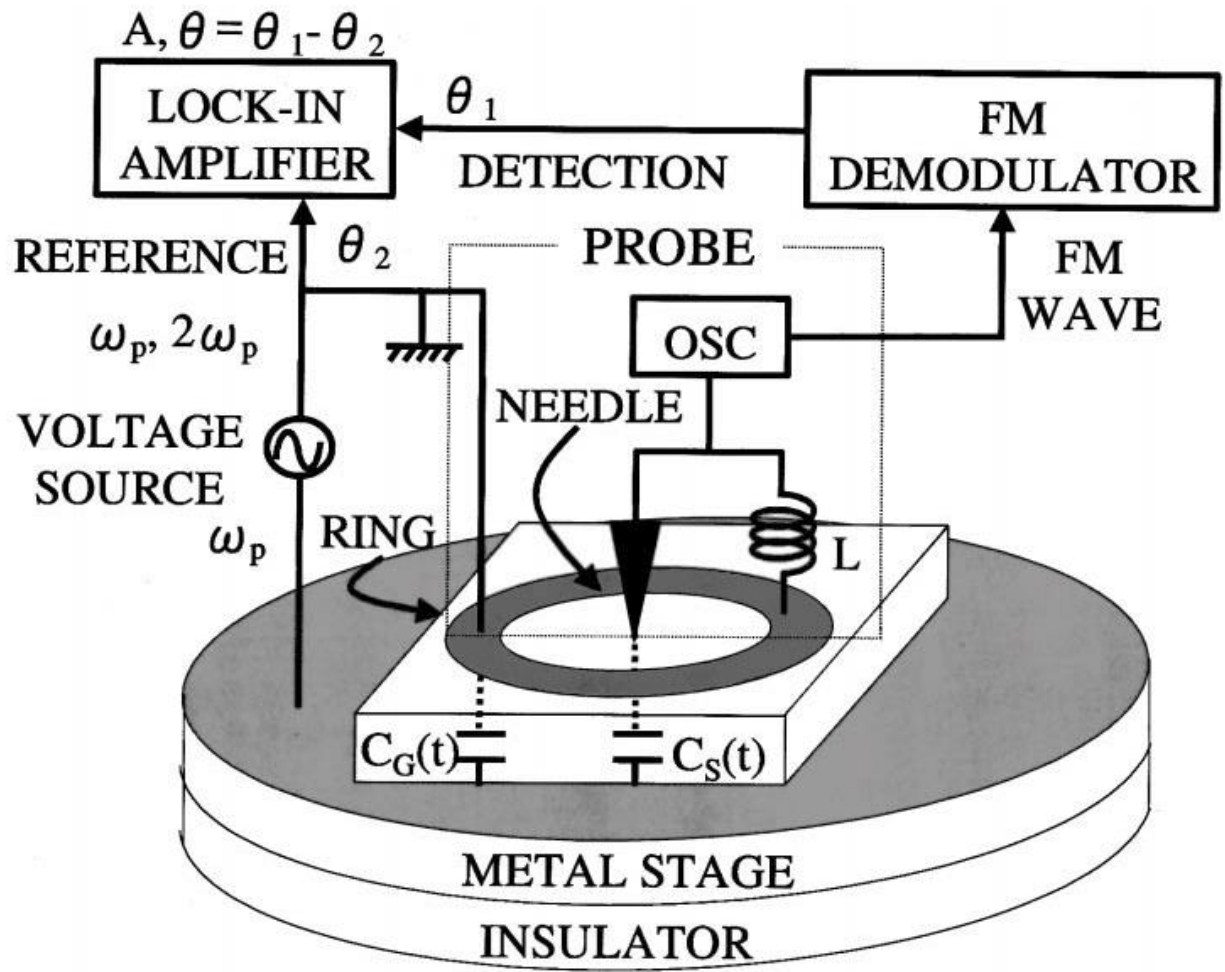


Figure 9.9

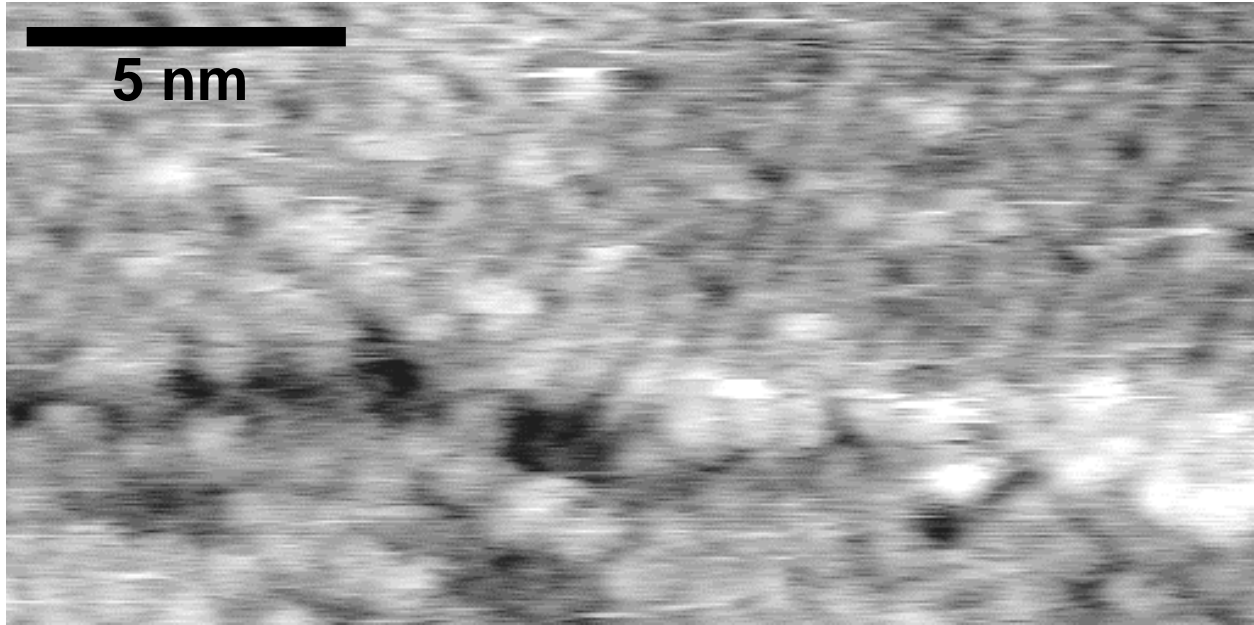


Figure 9.10

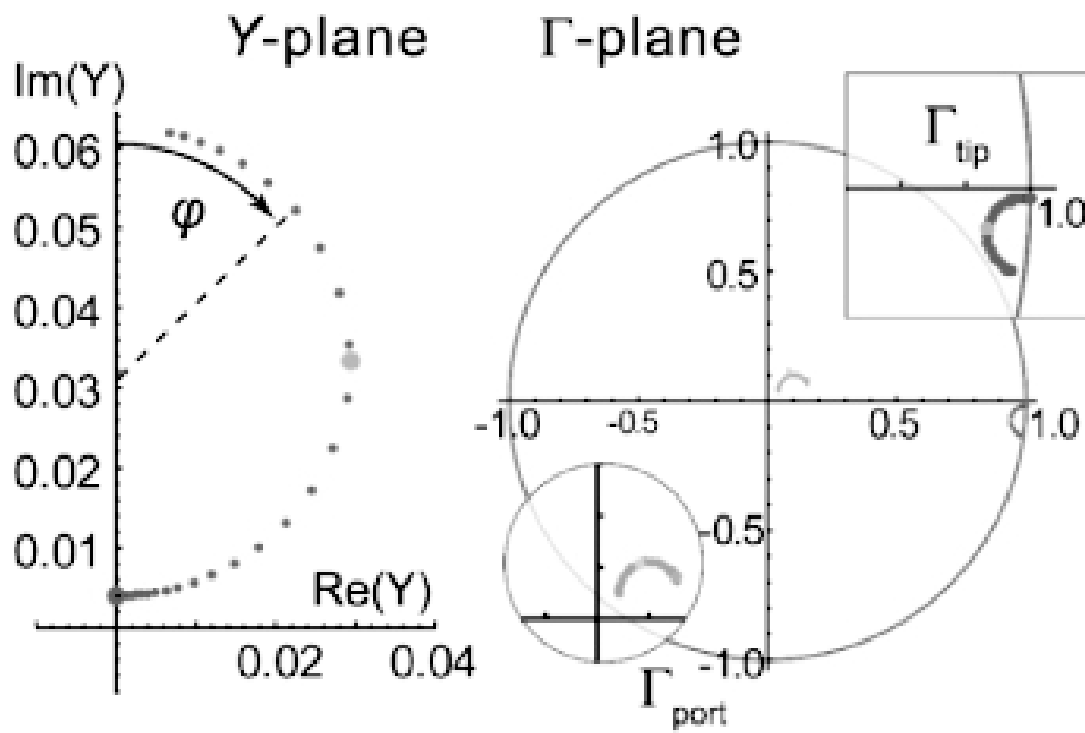


Figure 9.11

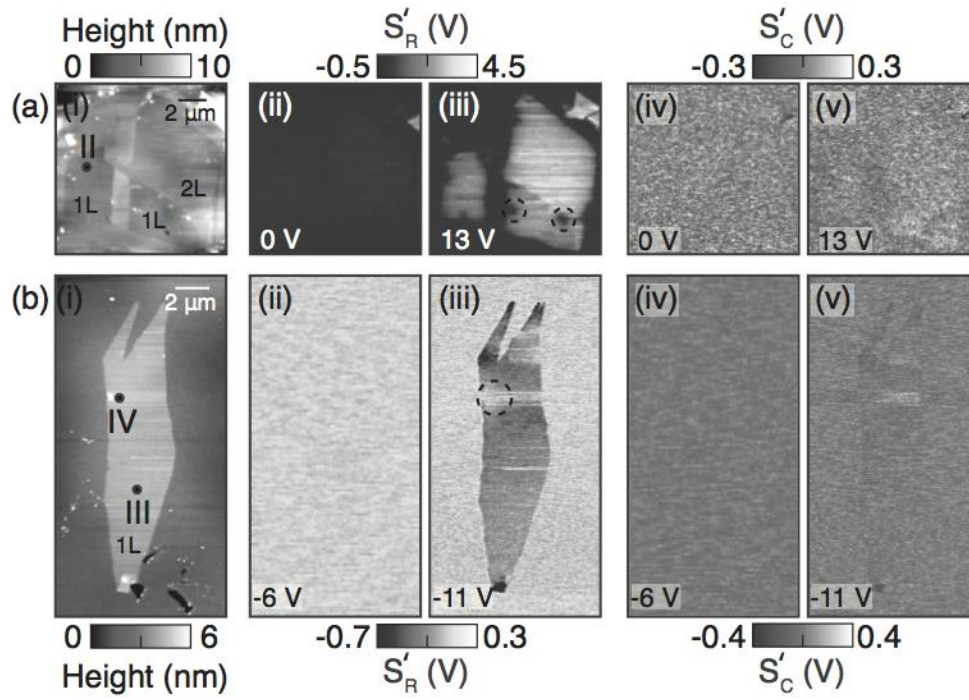


Figure 9.12

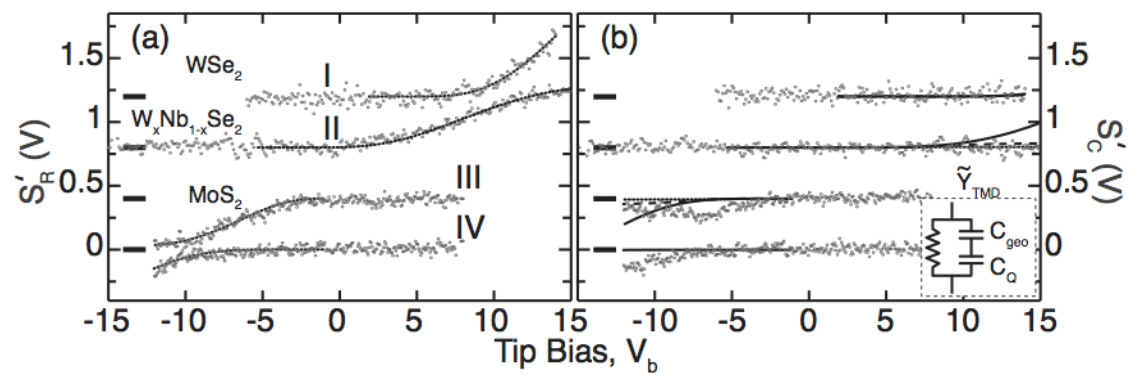


Figure 9.13